Coupled impacts of atmospheric circulation and sea-ice on late Pleistocene terrigenous sediment dynamics in the subarctic Pacific Ocean

Yi Zhong [1, 2, 3], Yanguang Liu [2, 4], Xun Gong [2, 5], David J. Wilson [6], Zhengyao Lu [7], Jiabo Liu [1, 2, 3], Tengfei Song [8], Sergey Gorbarenko [9], Xuefa Shi [2, 4], Xiaoqiang Yang [10], Qingsong Liu [1, 2, 3*]

[1] Centre for Marine Magnetism (CM^2), Department of Ocean Science and Engineering, Southern University of Science and Technology, Shenzhen 518055, PR China

[2] Laboratory for Marine Geology, Qingdao National Oceanography Laboratory for Marine Science and Technology, Qingdao 266061, PR China

[3] Southern Marine Science and Engineering Guangdong Laboratory (Guangzhou), Guangzhou, China

[4] Key Laboratory of Marine Geology and Metallogeny, First Institute of Oceanography, Ministry of Natural Resources (MNR), Qingdao 266061, China

[5] Hubei Key Laboratory of Marine Geological Resources, China University of Geosciences (Wuhan), Wuhan, 430074, China

[6] Institute of Earth and Planetary Sciences, University College London and Birkbeck, University of London, London, UK

[7] Department of Physical Geography and Ecosystem Science, Lund University, Lund, Sweden

[8] GEOTOP, Université du Québec à Montréal, C.P. 8888, Montréal, QC H3C 3P8, Canada

[9] V.I.Il‘ichev Pacific Oceanological Institute, Far East Branch of Russian Academy of Science, Vladivostok 690041, Russia

[10] Department of Earth Science, Sun Yat-Sen University, Guangzhou 510275, PR China

[*]Corresponding author: qsliu@sustech.edu.cn

Key Points:

Source-to-sink study in the subarctic Pacific Ocean based on geochemical, clay mineral, and environmental magnetic proxies.

Glacial/interglacial variablity is interpreted to result from atmospheric climatic modes linked to by Aleutian Low forcing.

Evidence for changes in the strength and location of North Pacific Intermediate Water formation through glacial-interglacial cycles.

Abstract

Processes controlling environmental change in the subarctic Pacific Ocean on millennial to orbital timescales are not well understood. Here we use a 230-kyr sedimentary record from the northwest Pacific Ocean to assess the response of late Pleistocene sediment dynamics to orbital forcing. Combining a source-to-sink perspective based on sedimentological records with climate model reanalysis, we reveal that fluctuations in sediment provenance were closely linked to obliquity-forced changes in atmospheric circulation modes. Specifically, the position of the Aleutian Low controlled sediment transport from the Bering Sea and Aleutian Arc sources. Furthermore, a distinct shift in North Pacific ocean circulation during the Last Glacial Maximum may have been related to a strengthened Siberian High. The coincidence of atmospheric mode switches with changes in sea-ice extent and North Pacific Intermediate Water formation in the marginal seas suggests that this coupled ocean-atmosphere system may have acted as a regional amplifier of global climate variability.

Plain Language Summary

We use a sedimentary record from the northwest Pacific Ocean to assess the sensitivity of regional sediment transport dynamics to orbital forcing over the last 230 thousand years. By combining the sedimentological records with climate model simulations, we suggest that changes in sediment transport could have resulted from obliquity-scale changes in atmospheric climatic modes, and specifically the position of the Aleutian Low. Moreover, we found a shift in the location of intermediate water formation during the Last Glacial Maximum, which may have been related to a strengthened Siberian High. This coupled ocean-atmosphere system represents a potential amplifier of climate variability, such that improved constraints on its past behavior could provide insight into how climatic signals are transferred between regional and global scales.

1. Introduction

The subarctic Pacific Ocean (SPO) provides a key connection between the low and high latitude climate systems and plays an important role in global climate change. For example, both Arctic sea-ice extent (Praetorius et al., 2018) and North Pacific Intermediate Water (NPIW) formation (Rae et al., 2020) are closely coupled to North Pacific hydroclimate. Therefore, climate variability in this region is strongly influenced by synoptic-scale ocean-atmosphere dynamics (Serno et al., 2017). In addition, the terrestrial hydroclimate influencing the North Pacific continental margins is sensitive to the position and intensity of the Aleutian Low, an atmospheric low-pressure cell centered on the Aleutian Islands that affects the strength and trajectory of winter storms (Nakanowatari et al., 2017; Rodionov et al., 2007). While recent observations (Litow et al., 2020) and paleoceanographic records (Broadman et al., 2020) demonstrate the coupled impacts of North Pacific atmospheric circulation and Arctic sea ice on the regional hydroclimate, little is known about the long-term dynamics of these atmospheric modes or their interaction with oceanic processes in the SPO.

Marine sediment cores from the SPO provide valuable evidence on paleoclimatic processes, including atmospheric and oceanic circulation patterns, weathering inputs, riverine discharge, and ice sheet behavior (Ovsepyan et al., 2017; Riethdorf et al., 2016). In this region, the Siberian High (SH; high atmospheric pressure over East Siberia) - Aleutian Low (AL; low atmospheric pressure over the Aleutian Arc) system has been proposed to exert a dominant control on Pleistocene glacial-interglacial cyclicity in sea ice, ocean circulation, and hydroclimate (Ovsepyan et al., 2017; Rodionov et al., 2007; Wu & Wang, 2002). In the modern climate, the SH-AL system controls the sea-ice distribution in the Bering Sea and the Sea of Okhotsk (Cavalieri & Parkinson, 1987) (Figure 1a). Acting as a part of the Pacific Decadal Oscillation, the SH-AL system also impacts on winter climate in western North America and the broader North Pacific region (Mantua et al., 1997; Minobe, 1997). In the marginal seas of the SPO, intensified sea-ice formation was associated with enhanced brine rejection and more active intermediate water production during the Pleistocene (Kender et al., 2019; Khim et al., 2012). Moreover, changes in the position and intensity of the AL regulated ocean circulation and depositional processes in the SPO over orbital timescales (Wang et al., 2017; Zou et al., 2015). As such, there is great potential to exploit sedimentary records to constrain the past operation of the SH-AL system. However, to date, paleoclimate datasets from this region have generally not been interpreted in the context of the coupled ocean-atmosphere system, and better constraints are needed on the changes in physical processes over orbital timescales. Understanding orbital-scale changes in the past ocean dynamics provides an important context for predicting future changes in Pacific-Arctic teleconnections and ocean-atmosphere dynamics (Broadman et al., 2020).

Here, we present geochemical data, clay and heavy mineral abundances, and rock magnetic records from core LV63-4-2 recovered from a water depth of 2,946 m in the SPO (Figure 1b). Our new data constrain changes in the provenance and transport of terrigenous sediments to the ocean on orbital timescales back to 230 ka BP. We determine that terrigenous sediment dynamics were driven by the intensity and position of the AL, which varied with obliquity forcing, and were also associated with fluctuations in Arctic sea-ice extent. We also present a data-model comparison, based on coupled atmosphere-ocean model simulations and sea-ice reconstructions, which supports our interpretation of the changes in terrigenous sediment dynamics. Overall, our data highlight a prominent glacial-interglacial shift in ocean circulation and sea-ice coverage in the region, as well as differences between the Last Glacial Maximum (LGM) and previous glacial episodes. Such results have implications for understanding the important role of both sea ice and high-latitude ocean-atmosphere dynamics in the past and future of the Arctic region.

2. Materials and methods

This study is based on a 6.88 m-long gravity core LV63-4-2 (water depth: 2,946 m; location: 51.63°N, 167.81°E) (Figure 1), which was recovered from the northern Emperor Seamounts during the Russian-Chinese joint expedition on the R/V *Akademik M.A. Lavrentyev* in 2013. The core is situated in the open western subarctic Pacific Ocean and full details of the regional setting are provided in the supplementary material (Text S1). The stratigraphic framework of LV63-4-2 is described in detail in a previous study (Zhong et al., 2020). Briefly, X-ray fluorescence (XRF) and spectrophotometric (color L^*) data were correlated to the oxygen isotope ($\delta^{18}O$) records from the North Greenland Ice Core Project (NGRIP) ice core (Barker et al., 2011) and the Sanbao stalagmites in China (Cheng et al., 2016). This approach was validated by planktonic foraminiferal $\delta^{18}O$ stratigraphy, magnetostratigraphy, tephrochronology, and accelerator mass spectrometry radiocarbon dating of planktonic foraminifera. Based on these data, core LV63-4-2 comprises the interval from 0 to 230 ka. Linear sedimentation rates vary between ~1 and ~19 cm/kyr (average of ~3 cm/kyr), while the uncertainty of the age model is fairly constant and on the order of ~5-10 kyr (2σ) throughout the core (Figure S1).

For this study, samples were taken at 1-3 cm intervals throughout the core to perform analyses of the clay minerals, light and heavy minerals, major elements, and magnetic minerals. The datasets therefore translate to millennial to sub-millennial-scale resolution. We also conducted spectral analysis to examine the periodicities in the mineralogical and magnetic proxy records. Full details of the analytical methods are provided in Text S2, and a description of the downcore mineralogical, chemical, and rock magnetic parameters is provided in Text S3.

We use reanalysis data from 1979 to 2017 to investigate the relationship between the AL location, low-level wind vector field, and sea-ice extent in the North Pacific marginal seas. The monthly atmospheric data are from National Centers for Environmental Predictions (NCEP) Reanalysis-2 (Kanamitsu et al., 2002), which has a 2.5-degree spatial resolution and 17 vertical levels. The monthly sea-ice concentration data are from the National Snow & Ice Data Center (NSIDC) Gridded Monthly Sea Ice Extent and Concentration, 1850 Onward, Version 2 (Walsh et al., 2019), which has a 1/4-degree spatial resolution.

3. Results

The sedimentological records of core LV63-4-2 reveal differences between glacial and interglacial periods (Figure S2-S3). In general, changes in clay mineralogy can be related to multiple factors, including parent rock mineralogy, weathering intensity, and diagenesis. In this setting, high smectite contents point to local sources from the altered volcanic rocks of the Aleutian Arc and Kamchatka (Naidu et al., 1995). Kamchatka is mostly characterised by Mesozoic and Cenozoic sedimentary rocks (Zonenshain et al., 1990), whereas the Aleutian Arc is composed of Cretaceous to recent andesites and basalts (Beikman, 1980). Another mineralogical province is confined to the northeastern continental margin of the Bering Sea and is characterised by high illite contents, with substantial chlorite and less smectite and kaolinite (Naidu et al., 1995).

Sediments can be supplied to that margin from the erosion of continental rocks, via the Yukon and Kuskokwim rivers of the Alaskan mainland and the Anadyr River in northeastern Siberia (Asahara et al., 2012).

Some previous studies suggested that aeolian particles from central Asia can play an important role in providing detrital fluxes to the pelagic Pacific Ocean (Nakai et al., 1993; Serno et al., 2014), so we compare the clay mineral data from core LV63-4-2 to reference data from Chinese loess (Wan et al., 2007), in addition to data from rivers from the northern continental margin of the Bering Sea and Aleutian and Kamchatka island arcs (Naidu et al., 1995). The majority of the samples in core LV63-4-2 plot as a tight cluster and do not coincide with the composition of Chinese loess sources (Figure 2). We therefore consider that the influence of aeolian particles on the sediment composition can be neglected, which is also supported by the relatively high sedimentation rate in core LV63-4-2. Hence, the clay mineral data are interpreted to reflect a mixture of sediment sources from old continental rocks via the large rivers of the Alaskan mainland and northeastern Siberia and young rocks of the Kamchatka and Aleutian arcs (Figure 2).

During glacial marine isotope stages (MIS) 2, 4, and 6, the clay mineral assemblages correspond to clay mineral data from the northern coast of the Bering Sea (Figures 2g-i), whereas there is a slight trend towards the composition of more smectite-rich sources from the Aleutian Arc and/or Kamchatka during interglacial stages MIS 1, 3, and 5 (Figures 2a-c). Such a glacial-interglacial provenance change is also supported by changes in quartz and volcanic glass content (Figures S3j and S3l). Specifically, lower smectite / (illite + chlorite) ratios during glacial periods (Figure 3c) were accompanied by significantly reduced inputs of volcanic glass, which decreased from ~60 % during interglacials to become almost absent in glacials (Figure 3d). Similarly, studies on surface sediments from the eastern Bering Sea shelf also indicate mixing between detrital material from the Yukon River and Aleutian Arc sources (Asahara et al., 2012; Nagashima et al., 2012). Moreover, the transport of clays from the Bering Sea to LV63-4-2 is consistent with isotopic provenance data on the silt-sized sediment fraction at the Meiji Drift, which indicate transport of sediment from the Bering Sea to the Northwest Pacific during the last glacial period (VanLaningham et al., 2009). In addition to these glacial-interglacial changes, a predominant 23 kyr periodicity is observed in the clay mineralogy records (Figure 3c and Figure 4a-b).

An accurate interpretation of source-to-sink provenance in marine sediment also requires constraints on sediment transport processes (Wan et al., 2010), which can be derived from the magnetic properties of sediments. In particular, fabric alignment coefficients, based on the magnitude and direction of anisotropy of magnetic susceptibility (AMS), have been widely used to reconstruct both the magnitude and direction of paleo-flow (Kissel et al., 2013; Nichols et al., 2020; Zheng et al., 2016). For a normal sedimentary magnetic fabric, K_3 is sub-vertical and perpendicular to the bedding plane (I_{mean} = 69.3°), and K_1 inclinations are relatively shallow (I_{mean} = 9.5°) (Figure S4), which are typical index values for a non-perturbed system after deposition (Kissel et al., 1997). The AMS ellipsoid is characteristically oblate and is controlled mainly by foliation (F >1.001), whereas the degree of anisotropy (P_j) has values from

1 to 1.08 for most samples (Figure S4 and S5). These observations are consistent with normal current-influenced sedimentation in the deep sea. Furthermore, our rock magnetic results suggest that magnetite is the dominant magnetic mineral in the core and it has weak crystalline anisotropy (Figure S3), so the orientation of the magnetite grains will be dominated by the alignment of their long axes (Kissel et al., 2010).

Based on the AMS results, we are therefore able to reconstruct bottom current orientations. For interglacials, flow was from NW-SE during MIS 1 and from NE-SW during MIS 3 and MIS 5 (Figure 2d-f). Glacial intervals were generally linked to flow from N-S, but the LGM was characterised by both N-S and W-E flow directions (Figure 2j-l). In addition, magnetic properties in core LV63-4-2 indicate stronger current strength (higher K_1-inclination; Figure 3g) and enhanced fluvial inputs derived from the Bering Sea shelf (higher χ_{ARM}/SIRM and S-ratio; Figure 3e and f) during glacial periods. These inferences for the glacial state are consistent with other studies from the SPO (VanLaningham et al., 2009), the Sea of Okhotsk (Okazaki et al., 2014; Wang et al., 2017), and the Bering Sea (Riethdorf et al., 2013). Notably, unlike the clay mineral records, a pronounced 41 kyr periodicity is recorded in the magnetic records (Figure 4c-f).

4. Discussion

4.1. Response of terrigenous sediment sources and transport to Aleutian Low dynamics

A key finding from core LV63-4-2 is that the glacial ocean circulation in the region had distinct patterns (Figure 2) and higher velocities (Figure 3g) compared to interglacial states. Furthermore, magnetic mineral proxies (Figure 3e-f) and reduced inputs of volcanic glass (Figure 3d) indicate enhanced glacial sediment transport from the Bering Sea, in agreement with previous provenance results from the last glacial period (VanLaningham et al., 2009). Together, our data suggest that glacial periods were characterized by stronger export of Bering Sea water (and associated sediments) into the open North Pacific Ocean at intermediate to deep depths. This interpretation is also consistent with independent evidence from carbon isotopes (Knudson & Ravelo, 2016) (Figure 3i) and Nd isotopes (Horikawa et al., 2010; Jang et al., 2017) (Figure 3j) in the glacial Bering Sea. The stronger glacial export of intermediate or deep waters has been attributed to brine rejection during intensive winter sea-ice formation in the Bering Sea (Rella et al., 2012; Worne et al., 2019), with our records suggesting a possible role for obliquity forcing (Figures 3 and 4). This feature, together with weak spectral power in the precession band, was also seen in ocean-atmosphere general circulation modelling, which attributed it to the influence of obliquity on mean annual and seasonal insolation gradients at high latitudes (Lee & Poulsen, 2009). Seasonal insolation forcing has been shown to influence atmospheric circulation and vapor transport, leading to significant changes in snowfall, and presumably ice volume (Lee & Poulsen, 2008).

A second feature of the LV63-4-2 record is the variability in the clay mineral assemblage, which displays a stronger 23 kyr periodicity (Figure 3c and Figure 4a-b). This observation points to an additional control by precessional forcing, which may be indicative of changes in tropical ocean-atmosphere interactions (Yamamoto et al., 2007; 2013). Modern observations indicate that the AL, as part of the Pacific Decadal

Oscillation (Mantua et al., 1997), is closely linked to both the tropical El Niño-Southern Oscillation (Liu et al., 2014) and to sea-ice dynamics in the North Pacific marginal seas (Cavalieri & Parkinson, 1987), indicating the potential for both low and high latitude forcing. Furthermore, changes in large-scale atmospheric climate modes provide a reasonable mechanistic explanation for the relationship between past changes in depositional patterns over the SPO and the position of the AL in the North Pacific (Anderson et al., 2016; Yamamoto et al., 2017). In this context, we explore how variability in atmospheric circulation regimes associated with the position and intensity of the AL (Deschamps et al., 2019) could provide a unifying explanation for the various changes in sediment sources and transport dynamics recorded in core LV63-4-2 through glacial-interglacial cycles (Figure 5).

4.2. Interglacial climate: dominant control by AL intensity

During the warm interglacial intervals of MIS 1, 5.1, 5.3, and 5.5 (Regime I), maxima in smectite / (illite + chlorite) ratios and volcanic glass proportions (Figures 3c and 3d) coincide with precessional maxima in Northern Hemisphere summer insolation (Figure 3a). Such a precessional cycle is also found in sea surface temperature (SST) records from the East China Sea, suggesting that the Kuroshio Current (Figure 1b) and East Asian Summer Monsoon were stronger during these warm interglacial periods (Vats et al., 2020). Therefore, the northward-flowing Kuroshio Current could represent a low-to-high latitude connection that drives warm, saline tropical waters into the cooler, fresher SPO (VanLaningham et al., 2009), thereby modifying the regional climate. In addition, regional precipitation in the SPO could be driven by local insolation, for example via sea-ice feedbacks (Muller & MacDonald, 2000). Both mechanisms could contribute to enhanced weathering intensity and/or increased erosional supply of weathered materials from Kamchatka and the Aleutian Islands (Figure 5a).

Following the above discussion, we propose that the terrigenous sediment input and transport dynamics characterizing Regime I were dominantly controlled by the intensity of the AL state. During warm intervals of higher boreal summer insolation, the AL is weak and shifted northwards (Figures 5a and d). In such a state, the intensified supply of warm moist air from the subtropical Pacific could lead to increased weathering in Kamchatka and the Aleutian Islands (Vats et al., 2020; Yamamoto, 2009). Modern observations suggest that these changes in the pressure gradient between the SH and AL did not significantly affect the regional sea-ice extent (Figure 5d). The opening of the Bering Strait during interglacials (Rohling et al., 2014) (Figure 3l) could additionally have contributed to the warmer and wetter conditions by enabling a stronger exchange of water masses between the Bering Sea and the Pacific Ocean (Riethdorf et al., 2016).

4.3. Glacial climate: dominant control by the interaction between the AL and NPIW processes

An important mechanism that may modulate surface water densities and thereby constrain the timing and location of intermediate water formation is the rejection of brine during sea-ice formation (Haley et al., 2008). Such a process is believed to be a dominant control on NPIW formation in the SPO (Talley, 1993). During glacial intervals with lower obliquity (Regime IIa), the AL becomes stronger in winter, presumably due to the increased temperature contrast between land and ocean (Ueshima et al., 2006). The strengthening and southeastwards movement of the AL (Rikiishi & Takatsuji, 2005) causes stronger geostrophic winds within the SH-AL system (Figures 5b and e). With the AL moved to the east and anomalously higher pressure affecting northeastern Siberia, stronger northerly winds prevail over the Bering Sea (Luchin et al., 2002; Rodionov et al., 2007) (Figure 5e). Such winds would have led to an incease in sea-ice extent over the Bering Shelf and across the Aleutian Basin (Figure 5b), causing intense brine rejection and the associated intermediate or deep-water ventilation in the northwestern Bering Sea (Kender et al., 2019). In parallel, a strengthening and southward shift of the Subarctic Front could restrict the transport of warmer and wetter air masses from the tropical Pacific (Gorbarenko et al., 2005).

During these glacial intervals, the magnetic mineral grain size is finer (high χ_{ARM}/SIRM; Figure 3e) and S-ratios are higher (Figure 3f), reflecting the nature and composition of continental riverine inputs supplied to the marginal seas. Such characteristics are also seen in the variability of rock magnetic properties in Pleistocene deep-sea sediments from the Bering Sea (Lund et al., 2021). The dominance of the strongest 41 kyr periodicity signal in studied magnetic record was evidenced by ETP curves and wavelet spectra of the parameters (Fig. 4c-f). The finer magnetic minerals are more strongly controlled by slope deposition or drift deposition linked to intermediate to deep-water flow, which lead to better sorted and finer-grained sedimentary sequences (Sommerfield et al., 2007). Transport of these sediments to the North Pacific indicates the effect of intensified brine rejection and intermediate or deep-water ventilation (Figure 3i-j) in the Bering Sea and the Sea of Okhotsk (Jang et al., 2017; Kim et al., 2015).

Although the magnetic proxies appear to be related to NPIW formation during glacial periods, the source regions for NPIW remain debated. For the LGM, some authors have proposed an occurrence of ventilation in the Bering Sea (Ohkushi et al., 2003; Rella et al., 2012), whereas others have argued that the Sea of Okhotsk remained the main contributor to NPIW formation (Max et al., 2014; Okazaki et al., 2014; Tanaka & Takahashi, 2005). Notably, a record of percent *Cycladophora davisiana* from the SPO (Tanaka & Takahashi, 2005) (Figure 3h), which reflects the oxygenation state in the intermediate-depth Pacific Ocean, does not correspond closely with ventilation reconstructions from the Bering Sea (Jang et al., 2017) (Figures 3i-j). Such a discrepancy could be resolved by variations in intermediate water production in the Bering Sea versus the Sea of Okhotsk and/or the Gulf of Alaska.

Our results from AMS direction measurements reveal two different glacial deep-water ventilation modes that were potentially associated with distinct sea-ice distributions. During glacials MIS 4 and 6, asociated with flow from N-S (Figures 2k-l), we propose that the dominant source region of intermediate water in the North Pacific switched to the Bering Sea (Regime IIa; Figure 5b). During the LGM, the variable direction of AMS (Figure 2j) suggests that there were source regions in both the Bering Sea and the Sea of Okhotsk (Regime IIb; Figure 5c), while the deep-water strength appears to have been stronger (Figure 3g). The persistence of a source from the Sea of Okhotsk at the LGM is also supported by the high abundance (~40%) of the radiolarian species *C. davisiana* in the SPO (Figure 3h) (Tanaka & Takahashi, 2005), which provides an indicator of cold, oxygen-rich intermediate waters, such as those found in the present-day Okhotsk Sea Intermediate Water (Itaki & Ikehara, 2004; Okazaki et al., 2003).

Changes in the mode of the AL, i.e. strengthened and/or located towards the east of the North Pacific (Figure 5b) versus weakened and/or located more to the west of the North Pacific (Figure 5a), exert a critical influence on winter winds and precipitation patterns (Barron et al., 2011). Moreover, Itaki and Ikehara (2004) suggested that the AL position shifted southwards from the early to the late Holocene, accompanied by an increased sea-ice coverage in the Sea of Okhotsk. The relationship between the AL, wind patterns, and sea-ice distributions can also be inferred from reanalysis data from 1979 to 2017 (Kanamitsu et al., 2002; Walsh et al., 2019). When the winter sea-ice extent in the Bering Sea reaches its maximum (Figure 5e, blue line), the AL is displaced eastwards (Figure 5e, blue label 'L') and there are strong northerly wind anomalies over the Bering Sea (Figure 5e, arrows). In contrast, southeasterly wind anomalies are established over the Sea of Okhotsk, which hinders sea-ice formation in that region (Figure 5e). Considering instead the situation when sea-ice in the Sea of Okhotsk reaches its maximum (Figure 5f, blue line), the AL is located relatively further west (Figure 5f, blue label 'L') and the local wind anomalies (Figure 5f, arrows) provide favourable condition for sea-ice transport in the Sea of Okhotsk.

During past glacial maxima of MIS 4 and MIS 6, we propose that the AL shifted to the east, inducing cold northerly winds that were favourable for sea-ice formation in the Bering Sea, while warm southeasterly winds prevented sea-ice expansion in the Sea of Okhotsk (Figures 5b and e). During the LGM, the progressive expansion of Arctic sea ice associated with the maximum Northern Hemisphere terrestrial ice volume (Figure 3k) could have caused an intensification and expansion of the SH, with the low-pressure AL shifting further eastwards (Figures 5c and 5f). Therefore, the enhancement of northerly winds could have led to dense water production and enhanced overturning in both the Sea of Okhotsk and the Bering Sea (Figures 5c and 5f).

5. Conclusions

Variability in wind directions, sea-ice formation, and hydrological budgets in the marginal seas adds complexity to understanding temporal and spatial changes in intermediate water production in the subpolar Pacific Ocean. By tracing terrigenous sediment sources and transport dynamics over orbital timescales, our study provides new constraints indicating the importance of the Aleutian Low dynamics as a potential feedback mechanism in high-latitude climatic and environmental changes. Although glacial-interglacial provenance changes in the subpolar Pacific Ocean appear to reflect the position of the Aleutian Low, as set by orbital forcing and glacial-interglacial climatic boundary conditions, further paleoceanographic studies will be required to explore more subtle differences indicated here between the different glacial periods. In particular, better constraints on the depths, source regions, and timing of overturning circulation changes in the North Pacific are needed in order to translate our qualitative findings into a more quantitative understanding of the impact of intermediate and deep water formation in the subpolar Pacific Ocean on both regional and global climate.

Acknowledgements

We thank Qingyou He (South China Sea Institute of Oceanology, Chinese Academy of Sciences) for helpful suggestions, and Xuguang Feng (First Institute of Oceanography, Ministry of Natural Resources) for software analysis. We also thank Dr. Valerie Trouet and two anonymous reviewers for their insightful input which helped us to improve the final manuscript. This work was supported financially by National Natural Science Foundation of China (Grants 41806063, 41874078, U1606401, and 4167605), Global change and Air-Sea Interaction (GASI-GEOGE-03), the Laboratory for Marine Geology, Qingdao National Laboratory for Marine Science and Technology (No. MGQNLM201818), SIGEPAX (No. 03F0704A), Shenzhen Science and Technology Program (KQTD20170810111725321), and 2020 Research Program of Sanya Yazhou Bay Science and Technology City (SKJC-2020-01-012). DJW is supported by a NERC independent research fellowship (NE/T011440/1). JBL is supported by the China Postdoctoral Science Foundation (2020M682770). See https://doi.org/10.5281/zenodo.5111468 for the datasets from this study.

References

Anderson, L., Berkelhammer, M., Barron, J. A., Steinman, B. A., Finney, B. P., Abbott, M. B. (2016). Lake oxygen isotopes as recorders of North American Rocky Mountain hydroclimate: Holocene patterns and variability at multi-decadal to millennial time scales. *Global and Planetary Change*, *137*, 131-148.

Asahara, Y., Takeuchi, F., Nagashima, K., Harada, N., Yamamoto, K., Oguri, K., & Tadai, O. (2012). Provenance of terrigenous detritus of the surface sediments in the Bering and Chukchi Seas as derived from Sr and Nd isotopes: Implications for recent climate change in the Arctic regions. *Deep Sea Research Part II: Topical Studies in Oceanography*, *61-64*, 155-171.

Barker, S., Knorr, G., Edward, R. L., Parrenin, F., Putnam, A. E., Skinner, L. C., et al. (2011). 800,000 years of abrupt climate variability. *Science*, *334*, 347-351.

Barron, J. A. & Anderson, L. (2011). Enhanced Late Holocene ENSO/PDO expression along the margins of the eastern North Pacific. *Quaternary International*, *235*, 3-12.

Beikman, H. M., (1980). Geologic map of Alaska. Scale 1:2,5000,000. U.S. Geological Survey, Arlington.

Berger, A. (1978). Long-term variations of caloric insolation resulting from the earth's orbital elements. *Quaternary Research*, *9*, 139-167.

Broadman, E., Kaufman, D. S., Henderson, A. C. G., Malmierca-Valeet, I., Leng, M. J., & Lacey, J. H. (2020). Coupled impacts of sea ice variability and North Pacific atmospheric circulation on Holocene hydroclimate in Arctic Alaska. *Proceedings* *of the National Academy of Sciences of the United States of America*, *117*(52), 33034-33042.

Cavalieri, D. J., & Parkinson, C. L. (1987). On the relationship between atmospheric circulation and the fluctuations in the sea ice extents of the Bering and Okhotsk Seas. *Journal of Geophysical Research: Oceans*, *92*, 7141-7162.

Cheng, H., Edwards, R. L., Sinha, A., Spötl, C., Yi, L., Chen, S., et al. (2016). The Asian monsoon over the past 640,000 years and ice age terminations. *Nature*, *534*, 640-646.

Deschamps, C.-E., Montero-Serrano, J.-C., St-Onge, G., & Poirier, A. (2019). Holocene changes in deep water circulation inferred from authigenic Nd and Hf Isotopes in sediment records from the Chukchi-Alaskan and Canadian Beaufort margins. *Paleoceanography and Paleoclimatology*, *34*, 1038-1056.

de Boer, B., van de Wal, R. S. W., Lourens, L. J., Bintanja, R. & Reerink, T. J. (2013). A continuous simulation of global ice volume over the past 1 million years with 3-D ice-sheet models. *Climate Dynamics*, *41*(5-6), 1365-1384.

Gorbarenko, S. A., Basov, I. A., Chekhovskaya, M. P., Southon, J., Khusid, T. A., & Artemova, A. V. (2005). Orbital and millennium scale environmental changes in the southern Bering Sea during the last glacial-Holocene: Geochemical and paleontological evidence. *Deep-Sea Research Part II:Tropical Studies in Oceanography*, *52*, 2174-2185.

Haley, B. A., Frank, M., Spielhagen, R. F., & Eisenhauer, A. (2008). Influence of brine formation on Arctic Ocean circulation over the past 15 million years. *Nature Geoscience*, *1*(1), 68-72.

Horikawa, K., Asahara, Y., Yamamoto, K., & Okazaki, Y. (2010). Intermediate water formation in the Bering Sea during glacial periods: Evidence from neodymium isotope ratios. *Geology*, *38*, 435-438.

Itaki, T., & Ikehara, K. (2004). Middle to late Holocene changes of the Okhotsk Sea Intermediate Water their relation to atmospheric circulation. *Geophysical Research Letters*, *31*, L24309.

Jang, K., Huh, Y., Han, Y. (2017). Authigenic Nd isotope record of North Pacific Intermediate Water formation and boundary exchange on the Bering Slope. *Quaternary Science Reviews*, *156*, 150-163.

Kanamitsu, M., Kumar, A., Juang, H. M. H., Schemm, J. K., Wang, W. Q., Yang, F. L., et al. (2002). NCEP dynamical seasonal forecast system 2000. *Bulletin of the American Meteorological Society*, *83*(7), 1019.

Kender, S., Aturamu, A., Zalasiewicz, J., Kaminski, M. A., & Williams, M. (2019). Benthic foraminifera indicate Glacial North Pacific Intermediate Water and reduced primary productivity over Bowers Ridge, Bering Sea, since the Mid-Brunhes Transition. *Journal of Micropalaeontology*, *38*, 177-187.

Khim, B. K., Sakamoto, T., & Harada, N. (2012). Reconstruction of surface water conditions in the central region of the Okhotsk Sea during the last 180 kyrs. *Deep Sea Research Part II: Topical Studies in Oceanography*, *61-64*, 63-72.

Kim, S., Khim, B.K., & Cho, H.G. (2015). Clay mineral stratigraphy during the last 2.4 Ma at IODP Exp. 323 Site U1343 in the Bering Sea. *Marine Geology*, *359*, 163-168.

Kissel, C., Laj, C., Lehman, B., Labyrie, L., & Bout-Roumazeilles, V. (1997). Changes in the strength of the Iceland-Scotland Overflow Water in the last 200,000 years: Evidence from magnetic anisotropy analysis of core SU90-33, *Earth Planetary Science Letters*, *152*, 25-36.

Kissel, C., Laj, C., Kienast, M., Bolliet, T., Holbourn, A., Hill, P., Kuhnt, W., & Braconnot, P. (2010). Monsoon variability and deep oceanic circulation in the western equatorial Pacific over the last climatic cycle: Insights from sedimentary magnetic properties and sortable silt, *Paleoceanography*, *25*(3), PA3215.

Kissel, C., Van Toer, A., Laj, C., Cortijo, E., & Michel, E. (2013). Variations in the strength of the North Atlantic bottom water during Holocene. *Earth and Planetary Science Letters*, *369*, 248-259.

Knudson, K. P. & Ravelo, A. C. (2016). North Pacific Intermediate Water circulation enhanced by the closure of the Bering Strait. *Paleoceanography*, *30*(10), 1287-1304.

Laskar, J., Robutel, P., Joutel, F., Gastineau, M., Correia, A. C. M., & Levrard, B. (2004). A long-term numerical solution for the insolation quantities of the Earth. *Astronomy&Astrophysics*, *428*(1), 261-285.

Lee, S. Y. & Poulsen, C. J. (2008). Amplication of obliquity forcing through mean annual and seasonal atmospheric feedbacks. *Climate of the Past*, *4*, 205-213.

Lee, S. Y. & Poulsen, C. J. (2009). Obliquity and precessional forcing of continental snow fall and melt: implications for orbital forcing of Pleistocene ice ages. *Quaternary Science Reviews*, *28*(25), 2663-2674.

Litow, M. A., Hunsicker, M. E., Bond, N. A., Burke, B. J., Cunningham, C. J., Gosselin, J. L., et al. (2020). The changing physical and ecological meanings of North Pacific Ocean climate indices. *Proceedings of the National Academy of Sciences of the United States of America*, *117*(14), 7665-7671.

Liu, Z. Y., Lu, Z. Y., Wen, X. Y., Otto-Bliesner, B. L., Timmermann, A., & Cobb, K. M. (2014). Evolution and forcing mechanisms of El Niño over the past 21,000 years. *Nature*, *515*, 550-553.

Luchin, V. A., Semiletov, I. P., & Weller, G. E. (2002). Changes in the Bering Sea region: atmosphere-ice-water system in the second half of the twentieth century. *Progress in Oceanography*, *55*, 23-44.

Lund, S., Mortazavi, E. Platzman, E. Kirby, M., Stoner, J. & Okada, M. (2021). Rock magnetic variability of quaternary deep-sea sediments from the Bering Sea and their environmental implications. *Deep Sea Research Part I: Oceanographic Research Papers*, *172*, 103487.

Mantua, N. J., Hare, S. R., Zhang, Y., Wallace, J. M., & Francis, R. C. (1997). A Pacific interdecadal climate oscillation with impacts on salmon production. *Bulletin of the American Meteorological Society*, *78*, 1069-1079.

Max, L., Lembke-Jene, L., Riethdorf, J. R., Tiedemann, R., Nürnberg, D., Kühn, H., et al. (2014). Pulses of enhanced North Pacific Intermediate Water ventilation from the Okhotsk Sea and Bering Sea during the last deglaciation. *Climate of the Past*, *10*(2), 591-605.

Minobe, S. (1997). A 50-70 year climatic oscillation over the North Pacific and North America. *Geophysical Research Letters*, *24*, 683-686.

Muller, R. A. & MacDonald, J. (2000). Ice ages and astronomical causes: Data, spectral analysis and mechanisms. Springer Praxis Books in Environmental Sciences, p. 318.

Nagashima, K., Asahara, Y., Takeuchi, F., Harada, N., Toyoda, S., & Tada, R. (2012). Contribution of detrital materials from the Yukon River to the continental shelf sediments of the Bering Sea based on the electron spin resonance signal intensity and crystallinity of quartz. *Deep Sea Research Part II: Topical Studies in Oceanography*, *61-64*, 145-154.

Naidu, A. S., Han, M. W., Mowatt, T. C., Wajda, W. (1995). Clay minerals as indicators of sources of terrigenous sediments, their transportation and deposition: Bering Basin, Russian-Alaskan Arctic. *Marine Geolog*y, *127*, 87-104.

Nakai, S. I., Halliday, A. N., & Rea, D. K. (1993). Provenance of dust in the Pacific Ocean, *Earth Planetary Science Letters*, *119*(1), 143-157.

Nakanowatari, T., Nakamura, T., Uchimoto, K., Nishioka, J., Mitsudera, H. & Wakatsuchi, M. (2017). Importance of Ekman transport and gyre circulation change on seasonal variation of surface dissolved iron in the western subarctic North Pacific. *Journal of Geophysical Research: Ocean*, *122*(5), 4364-4391.

Nichols, M. D., Xuan, C., Crowhurst, S., Hodell, D. A., Richter, C., Acton, G. D., & Wilson, P. A. (2020). Climate-induced variability in Mediterranean Outflow to the North Atlantic Ocean During the Late Pleistocene. *Paleoceanography and Paleoclimatology, 35*, e2020PA003947.

Ohkushi, K. Itaki, T. & Nemoto, N. (2003). Last Glacial–Holocene change in intermediate-water ventilation in the Northwestern Pacific. *Quaternary Science Reviews*, *22*(14), 1477-1484.

Okazaki, Y., Takahashi, K., Nakatsuka, T. & Honda, M. C. (2003). The production scheme of *Cycladophora davisiana* (Radiolaria) in the Okhotsk Sea and the northwestern North Pacific: implication for the paleoceanographic conditions during the glacials in the high latitude oceans. *Geophysical Research Letter*s, *30*(18), 159-171.

Okazaki, Y., Kimoto, K., Asahi, H., Sato, M., Nakamura, Y., & Harada, N. (2014). Glacial to deglacial ventilation and productivity changes in the southern Okhotsk Sea. *Palaeogeography, Palaeoclimatology, Palaeoecology*, *395*, 53-66.

Ovsepyan, E. A., Ivanova, E. V., Lembke-Jene, L., Max, L., Tiedemann, R., Nürnberg D. (2017). Penultimate and last glacial oceanographic variations in the Bering Sea on millennial timescales: Links to North Atlantic climate. *Quaternary Science Reviews*, *163*, 135-151.

Owens, W. B., & Warren, B. A. (2001). Deep circulation in the northwest corner of the Pacific Ocean. *Deep-Sea Research-Oceanographic Research Papers*, *48*, 959-993.

Praetorius, S., Rugenstein, M., Persad, G., & Caldeira, K. (2018). Global and Arctic climate sensitivity enhanced by changes in North Pacific heat flux. *Nature Communications*, *9*(1), 3124.

Rae, J. W. B., Gray, W. B., Wills, R. C. J., Eisenman, I., Fitzhugh, B., Fortheringham, M. et al. (2020). Overturning circulation, nutrient limitation, and warming in the Glacial North Pacific. *Science Advance*, *6*(50), eabd1654.

Rella, S. F., Tada, R., Nagashima, K., Ikehara, M., Itaki, T., Ohkushi, K. I., et al. (2012). Abrupt changes of intermediate water properties on the northeastern slope of the Bering Sea during the last glacial and deglacial period. *Paleoceanography*, *27*, PA3203.

Ren, J., Gersonde, R., Esper, O., & Sancetta, C. (2014). Diatom distributions in northern North Pacific surface sediments and their relationship to modern environmental variables. *Palaeogeography Palaeoclimatology Palaeoecology*, *402*, 81-103.

Riethdorf, J. R., Nürnberg, D., Max, L., & Tiedemann, R. (2013). Millennial-scale variability of marine productivity and terrigenous matter supply in the western Bering Sea over the past 180 kyr. *Climate of the Past*, *9*, 1345-1373.

Riethdorf, J. R., Thibodeau, B., Ikehara, M., Nürnberg, D., Max, L., Tiedemann, R., & Yokoyama, Y. (2016). Surface nitrate utilization in the Bering sea since 180 ka BP: Insight from sedimentary nitrogen isotopes. *Deep Sea Research Part II Topical Studies in Oceanography*, *125*, 163-176.

Rikiishi, K., & Takatsuji, S. (2005). On the growth of ice cover in the Sea of Okhotsk with special reference to its negative correlation with that in the Bering Sea. *Annals of Glaciology*, *42*, 380-388.

Rodionov, S. N., Bond, N. A., & Overland, J. E. (2007). The Aleutian Low, storm tracks, and winter climate variability in the Bering Sea. *Deep Sea Research Part II: Topical Studies in Oceanography*, *54*, 2560-2577.

Rohling, E. J., Foster, G. L., Grant, K. M., Marino, G., Roberts, A. P., Tamisiea, M. & E., Williams, F. (2014). Sea-level and deep-sea-temperature variability over the past 5.3 million years. *Nature*, *508*, 477-482.

Schiemann, R., Luethi, D. & Schaer, C. (2009). Seasonality and interannual variability of the Westerly Jet in the Tibetan Plateau region. *Journal of Climate*, *22*(11), 2940-2957.

Schlitzer, R. (2013). Ocean Data View, <http;//odv.awi.de> (accessed 04.02.13).

Schulz, M. & Mudelsee, M. (2002). REDFIT: Estimating red-noise spectra directly from unevenly spaced paleoclimatic time series. *Computers & Geoscience*, *28*, 421-426.

Serno, S., Winckler, G., Anderson, R. F., Hayes, C. T., McGee, D., Machalett, B., Ren, H. J., et al. (2014). Eolian dust input to the Subarctic North Pacific. *Earth and Planetary Science Letters*, *387*, 252-263.

Serno, S., Winckler, G., Anderson, R. F., Jaccard, S. L., Kienast, S. S., & Haug, G. H. (2017). Change in dust seasonality as the primary driver for orbital-scale dust storm variability in East Asia. *Geophysical Research Letters*, *44*, 3796-3805.

Sommerfield, C., Ogston, A., Mullenbach, B., Drakes, D., & Leithold, E. (2007). Oceanic dispersal and accumulation of river sediment. In: Continental Margin Sedimentation: from sediment transport to sequence stratigraphy, Special Pub 37, International Association of Sedimentologists, pp. 157-205.

Talley, L. D. (1993). Distribution and formation of North Pacific Intermediate Water, Journal Physical Oceanography, 23, 517-537.

Tanaka, S. & Takahashi, K. (2005). Late Quaternary paleoceanographic changes in the Bering Sea and the western subarctic Pacific based on radiolarian assemblages. *Deep Sea Research Part II Topical Studies in Oceanography*, *52*(16), 2131-2149.

Ueshima, T., Yamamoto, M., Irino, T., Oba, T., Minagawa, M., Narita, H., & Murayama, M. (2006). Long term Aleutian Low dynamics and obliquity-controlled oceanic primary production in the mid-latitude western North Pacific (Core MD01-2421) during the last 145,000 years. *Global and Planetary Change*, *53*, 21-28.

VanLaningham, S., Pisias, N. G., Duncan, R. A., & Clift, P. D. (2009). Glacial-interglacial sediment transport to the Meiji Drift, northwest Pacific Ocean: Evidence for timing of Beringian outwashing. *Earth and Planetary Science Letters*, *277*, 64-72.

Vats, N., Mishra, S. Singh, R. K. Gupta, A. K. & Pandey, D. K. (2020). Paleoceanographic changes in the East China Sea during the last ~400 kyr reconstructed using planktic foraminifera. *Global and Planetary Change*, *189*, 103173.

Walsh, J. E., Chapman, W. L., Fetterer, F. & Stewart, J. S. (2019). Gridded Monthly Sea Ice Extent and Concentration, 1850 Onward, Version 2. [Indicate subset used]. Boulder, Colorado USA. NSIDC: National Snow and Ice Data Center.

Wan, S. M., Li, A. C., Clift, P. D., & Stuut, J. W. (2007). Development of the East Asian monsoon: Mineralogical and sedimentologic records in the northern South China Sea since 20 Ma. *Palaeogeography, Palaeoclimatology, Palaeoecology*, *254*(3), 561-582.

Wan, S. M., Li, A. C., Clift, P. D., Wu, S. G., Xu, K. H., & Li, T. G. (2010). Increased contribution of terrigenous supply from Taiwan to the northern South China Sea since 3 Ma. *Marine Geology*, *278*, 115-121.

Wang, K. S., Shi, X. F., Zou, J. J., Kandasamy, S., Gong, X., Wu, Y. H., & Yan, Q. S. (2017). Sediment provenance variations in the southern Okhotsk Sea over the last 180 ka: Evidence from light and heavy minerals. *Palaeogeography, Palaeoclimatology, Palaeoecology*, *479*, 61-70.

Worne, S., Kender, S., Swann, G. E. A., Leng, M. J., & Ravelo, A. C. (2019). Coupled climate and subarctic Pacific nutrient upwelling over the last 850,000 years. *Earth and Planetary Science Letters*, *522*, 87-97.

Wu, B., & Wang, J. (2002). Winter Arctic Oscillation, Siberian High and East Asian Winter Monsoon. *Geophysical Research Letters*, *29*(19), 1897.

Yamamoto, M. (2009). Response of mid-latitude North Pacific surface temperatures to orbital forcing and linkage to the East Asian summer monsoon and tropical ocean–atmosphere interactions. *Journal of Quaternary Science*, *24*(8), 836-847.

Yamamoto, M., Yamamuro, M., & Tanaka, Y. (2007). The California current system during the last 136,000 years: response of the North Pacific High to precessional forcing. *Quaternary Science Reviews*, *26*(3), 405-414.

Yamamoto, M., Sai, H., Chen, M. T., Zhao, M. X. (2013). The East Asian winter monsoon variability in response to precession during the past 150000 yr. *Climate of the Past*, *9*(6), 2777-2788.

Yamamoto, M., Nam, S. I., Polyak, L., Kobayashi, D., Suzuki, K., Irino, T., & Shimada, K. (2017). Holocene dynamics in the Bering Strait inflow to the Arctic and the Beaufort Gyre circulation based on sedimentary records from the Chukchi Sea. *Climate Past*, *13*, 1111-1127.

Zheng, X., Kao, S., Chen, Z., Menviel, L., Chen, H., Du, Y., et al. (2016). Deepwater circulation variation in the South China Sea since the Last Glacial Maximum. *Geophysical Research Letters*, *43*, 8590-8599.

Zhong, Y., Liu, Y. G., Yang, X. Q., Zhang, J., Liu, J. B., Bosin, A., et al. (2020). Do-non-dipole geomagentic field behaviors persistently exsit in the subarctic Pacific Ocean over the past 140 ka? *Science Bulletin*, *65*, 1505-1507.

Zonenshain, L. P., Kuzmin, M. I., & Natapov, L. M. (1990). Koryak-Kamchatka foldbelt. In: Page, B.M. (Ed.), Geology of the U.S.S.R.: a plate-tectonic synthesis. American Geophysical Union, Washington, D.C., pp. 149-167.

Zou, J. J., Shi, X. F., Zhu, A. M., Chen, M.-T., Kao, S. J., Wu, Y. H., et al. (2015). Evidence of sea ice-driven terrigenous detritus accumulation and deep ventilation changes in the southern Okhotsk Sea during the last 180 ka. *Journal of Asian Earth Sciences*, *114*, 541-548.

Figure Captions

Fig. 1

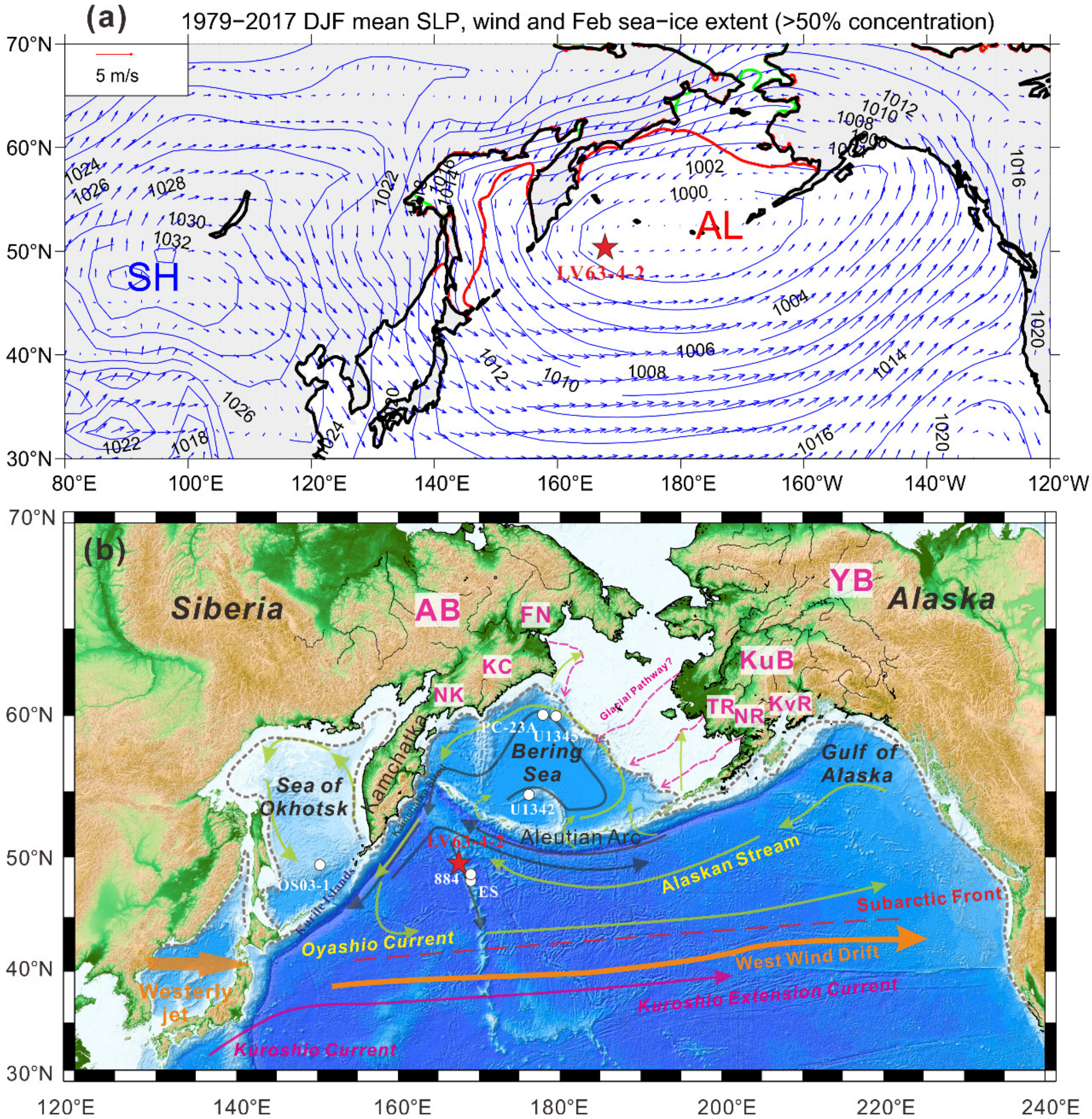

Figure 1. (a) Mean winter climate in the North Pacific based on reanalysis data from 1979 to 2017 (Kanamitsu et al., 2002; see main text for details). Blue contours show mean February sea level pressure (SLP) and blue arrows show mean December-January-February (DJF) 850-1000 hPa wind. Labels SH (Siberian High) and AL (Aleutian Low) depict the highest and lowest sea level pressure. Red and green lines show mean February and annual mean sea-ice extent (based on >50% concentration)

(Walsh et al., 2019). (b) Bathymetric chart of the subarctic North Pacific region, showing core sites, schematic ocean currents, and major river systems. The core site LV63-4-2 is from this study (red star). Previously studied cores (white circles) are the Sea of Okhotsk core OS03-1 (Wang et al., 2017), North Pacific cores ES (Tanaka & Takahashi, 2005) and ODP 884 (VanLaningham et al., 2009), and Bering Sea cores U1345 (Jang et al., 2017), U1342 (Knudson & Ravelo, 2016), and PC-23A (Rella et al., 2012). The surface circulation pattern (yellow arrows), Subarctic Front (red dashed line), Kuroshio Current and Extension (red arrows), and glacial pathways (dashed pink lines) are modified after VanLaningham et al. (2009) and Ren et al. (2014). Deep currents (black arrows) are based on Owens et al. (2001). The main path of the westerly jet stream (brown arrow) is based on Schiemann et al. (2009). Rivers and river basins from Siberia, following VanLaningham et al. (2009), are: AB = Anadyr River Basin; FN = far northeast Russia; KC = Koryak coastal basins; NK = Northern Kamchatka. Rivers and river basins from Alaska, following VanLaningham et al. (2009) and further differentiated, are: YB = Yukon River Basin; KuB = Kuskokwim River Basin; KvR = Kvichak River; NR = Nushagak River; TR = Togiak River. Grey dashed line indicates the LGM shoreline (~-120 m).

683 **Fig. 2.**

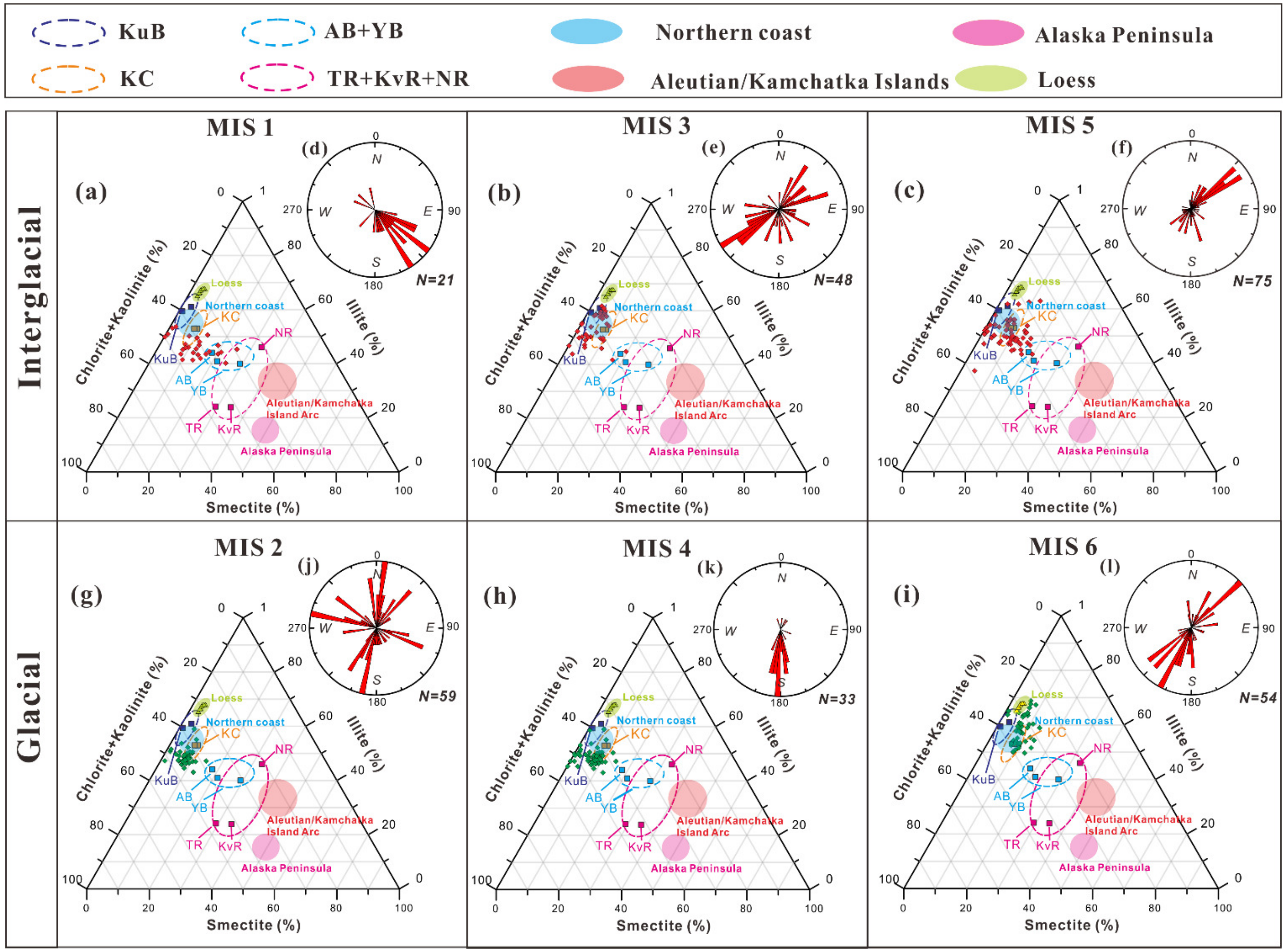

KuB
AB+YB
Northern coast
Alaska Peninsula
KC
TR+KvR+NR
Aleutian/Kamchatka Islands
Loess
Interglacial
Glacial
MIS 1
MIS 3
MIS 5
MIS 2
MIS 4
MIS 6
(a)
(b)
(c)
(d)
(e)
(f)
(g)
(h)
(i)
(j)
(k)
(l)
N=21
N=48
N=75
N=59
N=33
N=54
Chlorite+Kaolinite (%)
Illite (%)
Smectite (%)
Loess
Northern coast
KC
NR
KuB
AB
YB
TR
KvR
Aleutian/Kamchatka Island Arc
Alaska Peninsula

684

Figure 2. Clay mineralogy and magnetic susceptibility directions during different time intervals. (a-c, g-i) Ternary plots of smectite – illite – (chlorite + kaolinite) showing the provenance of clay minerals in core LV63-4-2 during (a-c) interglacial periods (red symbols), and (g-i) glacial periods (green symbols). Large dashed circles show clay mineral compositions of rivers, based on Naidu et al. (1995). KuB: Kuskokwim River Basin, KC: Koryak coastal basins, AB: Anadyr River Basin, YB: Yukon River Basin, TR: Togiak River, KvR: Kvichak River, NR: Nushagak River. Large solid circles represent offshore clay mineral compositions proximal to the northern coast of the Bering Sea (i.e., the Koryak Mountains and eastern Siberia), the Aleutian Islands/Kamchatka Arc, and the Alaska Peninsula (Naidu et al., 1995). The clay mineral compositions from Chinese loess are based on Wan et al. (2007). (d-f, j-l) Rose diagrams indicating the direction of anisotropy of magnetic susceptibility (AMS) for core LV63-4-2 during (d-f) interglacial periods, and (j-l) glacial periods. The number of samples in each interval (N) is also indicated for the magnetic data.

Fig. 3.

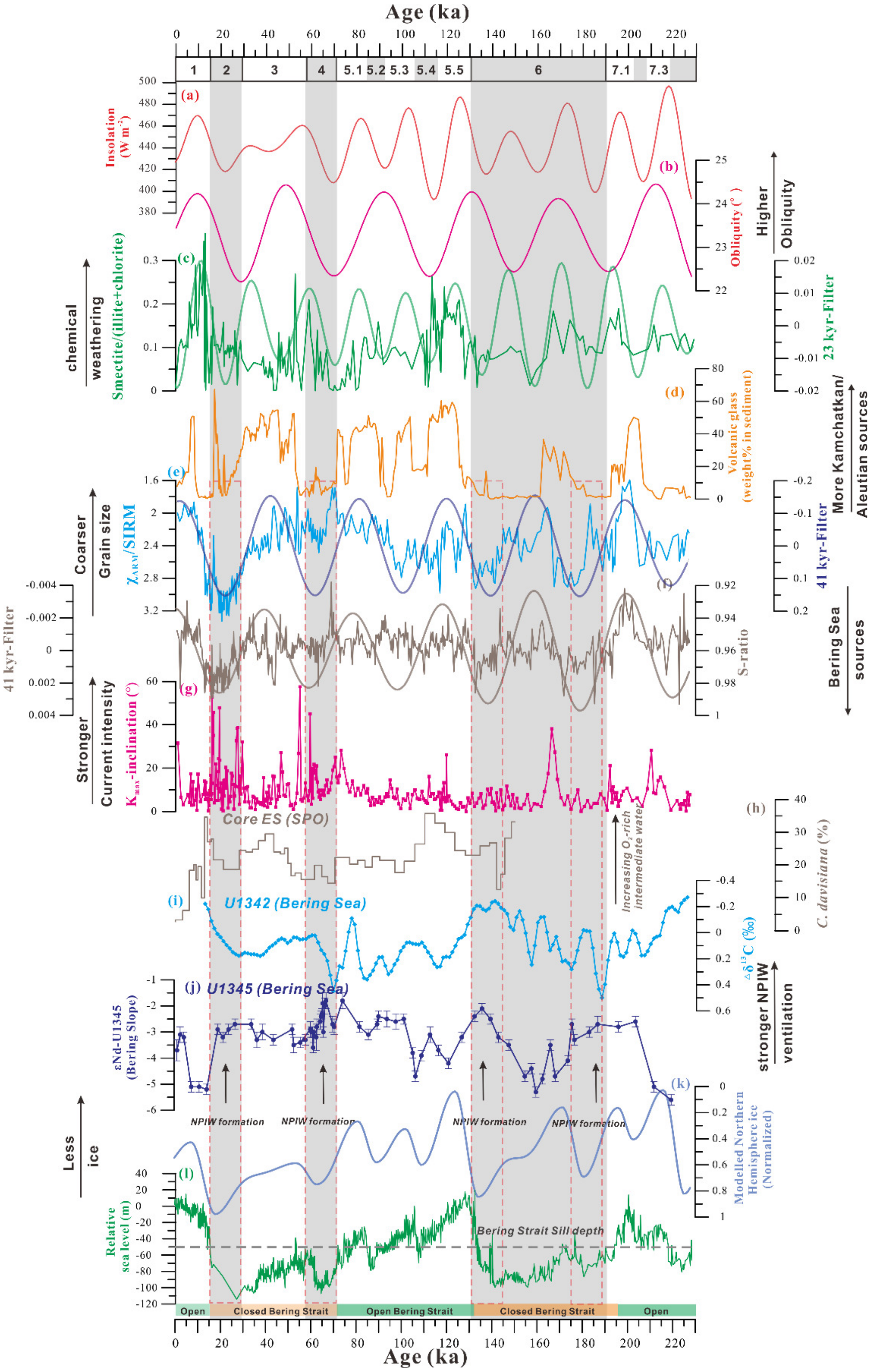

Figure 3. Proxy records from core LV63-4-2 in comparison to insolation forcing and other regional and global records over the past 230 ka: (a) Northern Hemisphere

summer insolation (65° July-September) (Laskar et al., 2004); (b) obliquity (Berger, 1978); (c) smectite / (illite + chlorite) ratio in core LV63-4-2, and 23 kyr Gaussian bandpass filtered output (thick green line); (d) volcanic glass weight percent of detrital grains in core LV63-4-2; (e) χ_{ARM}/SIRM in core LV63-4-2, and 41 kyr Gaussian bandpass filtered output (thick blue line); (f) S-ratio in core LV63-4-2, and 41 kyr Gaussian bandpass filtered output (thick grey line); (g) inclination of K_{max} from core LV63-4-2; (h) percent *Cycladophora davisiana* in Pacific core ES, as an indicator of intermediate water oxygenation (Tanaka & Takahashi, 2005); (i) carbon isotope gradient ($\Delta\delta^{13}C_{849\text{-}U1342}$) between Pacific Ocean (ODP 849) and Bering Sea (U1342) cores, as a proxy for NPIW ventilation (Knudson & Ravelo, 2016); (j) neodymium isotope (εNd) reconstruction from sediment leachates in Bering Sea core U1345, with more radiogenic values (arrows) interpreted to indicate NPIW formation in the Bering Sea (Horikawa et al., 2010; Jang et al., 2017); (k) Northern Hemisphere modelled ice volume (de Boer et al., 2013); (l) relative sea level (Rohling et al, 2014), compared to the sill depth of the Bering Strait (~50 m; dashed grey line), with green and orange bars indicating the approximate timings of an open versus closed Bering Strait. Grey vertical bars indicate glacial MIS 2, 4, and 6. Pink dashed outlines on panels (e-l) indicate intervals when enhanced NPIW formation is inferred. Note that some panels have reversed y-axes, while most have arrows and labels indicating simplified interpretations of the records.

Fig. 4.

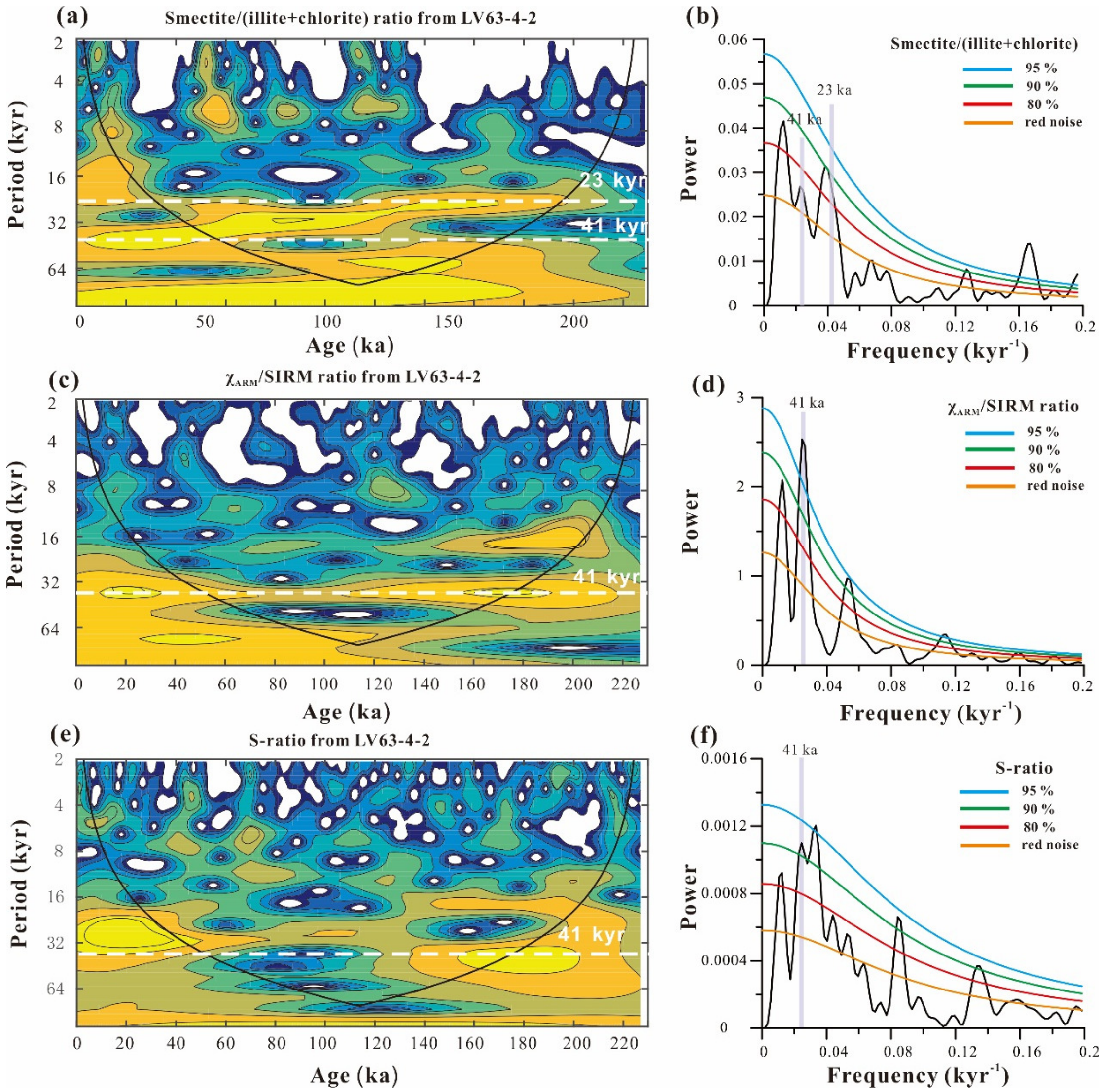

Figure 4. Time series analysis on clay mineralogy and magnetic properties in core LV63-4-2. Left panels show wavelet diagrams for (a) smectite / (illite + chlorite) ratio; (c) χ_{ARM}/SIRM ratio; and (e) S-ratio. The solid black contour lines identify regions where spectral power meets the 5% significance level against red noise, while the thick black line indicates the cone of influence. Dashed white lines indicate 41 kyr and 23 kyr periods. Right panels show the spectral power based on the REDFIT method (Schulz & Mudelsee, 2002) for (b) smectite / (illite + chlorite) ratio; (d) χ_{ARM}/SIRM

ratio; and (f) S-ratio. The orange, red, green, and blue lines indicate the first-order autoregressive (AR1) red noise model fit, 80% confidence level, 90% confidence level, and 95% confidence level, respectively. Grey shaded vertical bars indicate the frequencies related to 41 kyr and 23 kyr periods.

Fig. 5.

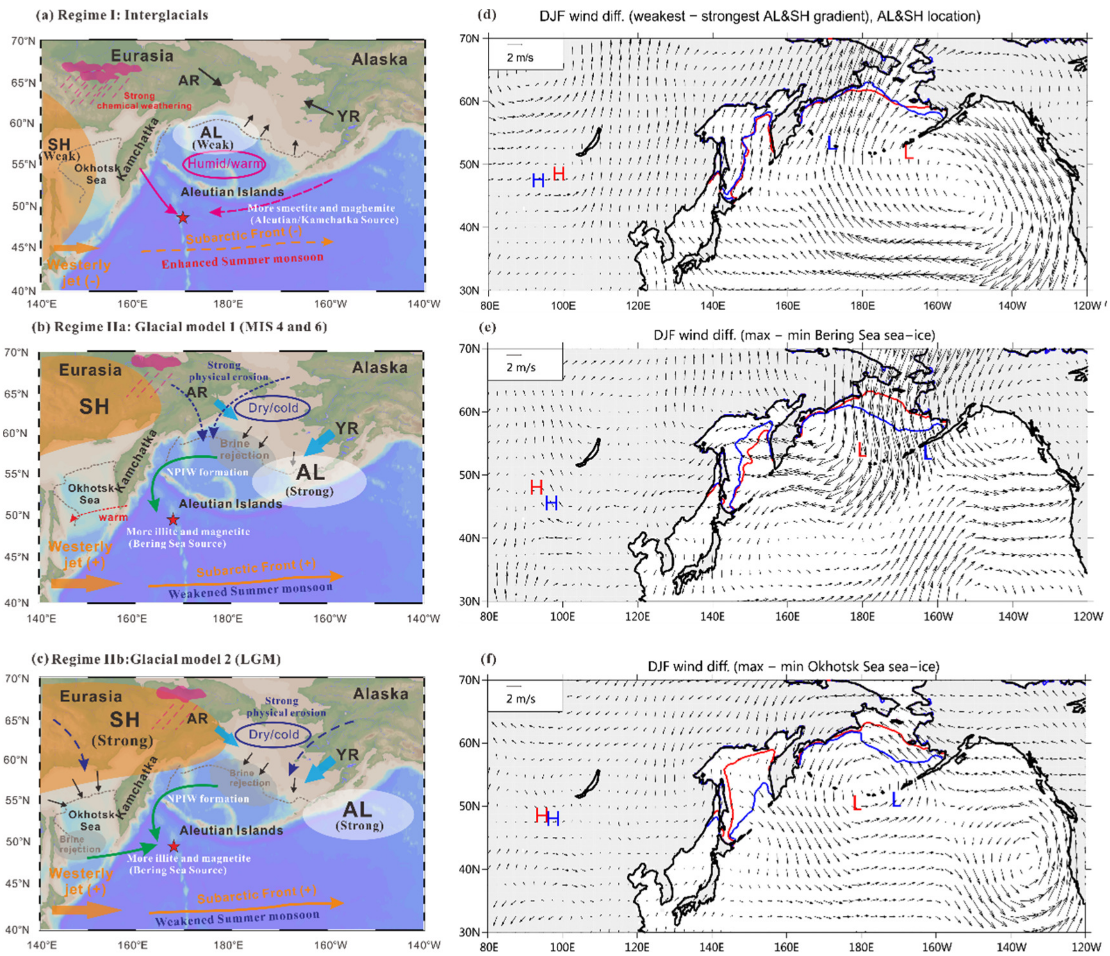

Figure 5. (a-c) Schematic illustration of the proposed influence of atmospheric circulation patterns on sea-ice extent, NPIW formation, and sediment provenance in the SPO over orbital timescales. (a) Regime I: warm interglacial state, characterised by enhanced chemical weathering intensity in the Aleutian Islands and Kamchatka, reduced sea-ice extent, and decreased sediment transport to core LV63-4-2 from the Bering Sea. (b) Regime IIa: cold glacial states (MIS 4 and MIS 6), characterised by reduced chemical weathering intensity, enhanced sea-ice formation in the Bering Sea, and increased sediment transport from the Bering Sea to core LV63-4-2 linked to NPIW formation. (c) Regime IIb: cold glacial states with an expanded SH (e.g. Last Glacial

Maximum, LGM), characterised by enhanced sea-ice formation in both the Bering Sea and Sea of Okhotsk, leading to two pathways of sediment transport by NPIW. Grey dashed lines, sea-ice extents in the Bering Sea and Sea of Okhotsk. Black arrows, extent of sea-ice advance or retreat. Grey patches, regions of brine rejection. Red arrows, sediment supply from Kamchatka and the Aleutian Islands. Blue dashed arrows, physical erosion inputs to the marginal seas. Large blue solid arrows, riverine inputs from the Anadyr River Basin (AR) and Yukon River Basin (YR). Green arrows, transport by NPIW. Large orange arrow, main path and direction of westerly jet stream (Schiemann et al., 2009). Thin orange arrow (solid or dashed), position and strength of Subarctic Front. Maps were created with Ocean Data View software (Schlitzer, 2013). (d-f) Reanalysis data from 1979-2017 (Kanamitsu et al., 2002; Walsh et al., 2019) showing 5-year composites of February sea-ice extent, winter (DJF) AL and SH locations (markers L and H), and differences in low-level (850-1000 hPa) wind (arrows) between the two states. (d) weakest (blue) and strongest (red) SH versus AL pressure gradient; (e) maximum (blue) and minimum (red) Bering Sea sea-ice extent; (f) maximum (blue) and minimum (red) sea-ice extent in the Sea of Okhotsk. See main text for further details and references. The corresponding composite wind patterns can be found in Fig. S6.

760

Geophysical Research Letters

Supporting Information for

Coupled impacts of atmospheric circulation and sea-ice on late Pleistocene terrigenous sediment dynamics in the subarctic Pacific Ocean

Yi Zhong[1,2,3], Yanguang Liu[2,4], Xun Gong[2,5], David J. Wilson[6], Zhengyao Lu[7], Tengfei Song[8], Jiabo Liu[1,2,3], Sergey Gorbarenko[9], Xuefa Shi[2,4], Xiaoqiang Yang[10] & Qingsong Liu[1,2,3*]

[*]Corresponding author: Email: qsliu@sustech.edu.cn

This PDF file includes:

Supplementary Text S1 to S3

Figures S1 to S6

Table S1

Introduction

The supporting information contains the Text S1 to S3, Figures S1 to S6, and Table S1. The Text S1 to S3 includes information on the regional setting, analytical methods (clay mineralogy, major elements, rock magnetic properties, light and heavy minerals, and spectral analysis), and an extended description of the sedimentological results.

Text S1 Regional Setting

The North Pacific Ocean is subdivided by the Subarctic Front into the Subarctic Gyre and the Subtropical Gyre (Qiu, 2002) (Figure 1b). The Subarctic Front, located between 40°N and 44°N in the western and central North Pacific, is characterised by an abrupt change in temperature and salinity where the cold, fresh water of the Subarctic Gyre to the north meets the warm, salty subtropical waters to the south (Yuan & Talley, 1996). South of the Subarctic Front, the Kuroshio Extension is an eastward extension of the Kuroshio Current (Qiu, 2002) and constitutes the northwestern boundary current of the Subtropical Gyre (Nakanowatari et al., 2017). The Subarctic Gyre consists of two sub-gyres, the Alaska Gyre in the east and the Western Subarctic Gyre in the west (Stabeno et al., 2016). The northern rim of the Alaska Gyre is the Alaskan Stream, which flows southwestwards along the Aleutian Islands, and transports fresh North Pacific surface waters into the Bering Sea mainly through gaps between the western Aleutian Islands (Naidu et al., 1995). Circulation in the Bering Sea is dominated by the Bering Sea Gyre, a large-scale cyclonic gyre that follows the continental slope (Danielson et al., 2014). The Bering Slope Current flows northwards along the shelf-slope break and bifurcates at around 58°N (Stabeno & Bell, 2019). Similarly, the Okhotsk Gyre is a cyclonic gyre that dominates the surface current system in the Sea of Okhotsk. A part of the surface water flows back into the North Pacific to form the Oyashio Current (Kwon et al., 2010).

Deep water exchange between the Bering Sea and the North Pacific occurs through the Kamchatka Strait (~4,000 m sill depth) and the Near Strait (~2,000 m sill depth)

(Figure 1b). In the present-day, a small amount of deep-water forms in the Bering Sea by brine rejection during winter sea-ice formation (Schlung et al., 2013). These deep waters flow southwards out of the Bering Sea into the northwestern Pacific Ocean through the Kamchatka Strait at depths below ~3000 m, whereas above these depths the predominant flow through the Strait is a northeastward inflow from the Pacific Ocean (Stabeno et al., 1999).

Sea-ice formation in the Bering Sea, and its advance and retreat, is strongly influenced by atmospheric circulation (Roden, 1995). In summer, the Bering Sea is bounded by the northern portions of a high-pressure system over the North Pacific and by a low-pressure system over Asia, resulting in weak pressure gradients and winds. In contrast, in winter, a low-pressure system dominates the North Pacific in the form of the Aleutian Low, with low atmospheric pressure centered on the Aleutian Islands (Niebauer et al., 1999) (Figure 1a). Vigorous air-sea exchange associated with cold air outbreaks and sea-ice formation in polynyas can locally increase surface water salinity up to 35‰ (Schumacher et al., 1983), leading to the formation of dense deep waters, and contributing to the cold halocline layer in the Aleutian Basin (Cavalieri & Marin, 1994). During anomalously cold winters, the Aleutian Low is displaced eastwards from its normal position, leading to more northerly winds and a southwards extension of the sea-ice region (Luchin et al., 2002).

Two main processes are responsible for terrigenous sediment supply to the North Pacific Ocean: long-distance aeolian sediment supply to the pelagic realm, and hemipelagic sediment dispersal from more proximal terrestrial sources via ocean currents flowing along ocean margins (Wang et al., 2016). However, aeolian transport of terrigenous materials to the North Pacific is largely restricted to the vicinity of the respective source areas (Riethdorf et al., 2016) and aeolian sediment accumulation rates are low elsewhere. Therefore, the major sedimentary sources to the core site of LV63-4-2 are continental inputs from the river basins of Siberia and Alaska and volcanic sediments from Kamchatka and the Aleutian Islands (Figure 1b). The major rivers are the Yukon and Kuskokwim rivers of Alaska, and the Anadyr River of Siberia, which contribute suspended sediment of 60, 8, and 2 million tons per year of suspended sediment, respectively (Riethdorf et al., 2016). The eastern Bering Sea shelf and slope sediments largely consist of reworked sand-sized sediment originally supplied by the Yukon River, whereas clay- and silt-sized particles are mostly restricted to the northeastern shelf, where they are directly supplied by the Yukon River (Nagashima et al., 2012).

Text S2 Methods

Clay mineralogy

A total of 232 samples from core LV63-4-2 were analysed for their clay mineralogy using X-ray diffraction (XRD). Clay minerals in the < 2 μm fraction were separated by settling according to Stokes' law, after removal of organic matter and carbonate by treatment with hydrogen peroxide (15%) and acetic acid (25%). The clay minerals were analyzed by XRD using a Dmax 2500 diffractometer with CuKα radiation (40 kV, 40 mA) at the Key Lab of Marine Sedimentology and Environmental

Geology, Ministry of natural resources, China. Identification of clay minerals was made according to the position of the (001) series of basal reflections on the three XRD diagrams (Moore & Reynolds, 1989). Semi-quantitative estimates of clay mineral abundance were conducted on glycolated samples based on the peak areas of the basal reflection for the major clay mineral groups (smectite-17 Å, illite-10 Å, and kaolinite/chlorite-7 Å). We used Topas 2P software with the empirical factors of Biscaye (1965), and the semi-quantitative abundances for each clay mineral have an accuracy of ~ 5%.

Elemental analysis

Core LV63-4-2 was scanned in the Core Processing Laboratory at the Key Lab of Marine Sedimentology and Environmental Geology (MASEG), State Oceanic Administration (SOA), using a non-destructive Avaatech X-ray fluorescence (XRF) Core Scanner. Split core surfaces were scanned at high resolution (0.5 cm spacing) during 50 kV and 10 kV runs, in order to obtain reliable intensities (counts per second) of the major elements Al, Si, Ti, Ca, Fe, K, Zr, Rb, Sr, and Ba.

Environmental magnetic analysis

A total of 334 paleomagnetic samples were collected using a standard 2 × 2 × 2 cm^3 plastic cube at 2 cm intervals along a fiducial line that was drawn prior to sampling. Low-field magnetic susceptibility (χ), magnitude and direction of the anisotropy of magnetic susceptibility (AMS), anhysteretic remanent magnetization (ARM), isothermal remanent magnetization (IRM), and characteristic remanent magnetization (ChRM) analyses were previously reported by Zhong et al. (2020).

The S-ratio and L-ratio were obtained from the following procedure. A saturation isothermal remanent magnetization was imparted in a 1.5 T applied field, termed $SIRM_{1.5T}$, then samples were demagnetized with backfields of -100 and -300 mT, and the corresponding remanences were measured, termed IRM_{-100mT} and IRM_{-300mT}. $HIRM_{300mT}$ is defined as $0.5 \times (SIRM_{1.5\,T} + IRM_{-300mT})$ and the S-ratio is defined as $-IRM_{-300mT}/SIRM_{-1.5T}$ (King & Channell, 1991). The HIRM and S-ratio can be used to quantify the absolute and relative concentrations of antiferromagnetic minerals (usually hematite and/or goethite), respectively. The L-ratio is defined as $(SIRM + IRM_{-300mT}) / (SIRM + IRM_{-100mT})$, and provides an indicator of how the hardness of hematite affects HIRM and S-ratio (Liu et al., 2007).

Magnetic fabric

The magnetic fabric and grain alignment in a sample can be estimated from the AMS, which is a susceptibility ellipsoid with three orthogonal principal axes, designated as the maximum (K_1), intermediate (K_2), and minimum (K_3) susceptibility axes (Hrouda, 1982). In this study, we examined the magnetic lineation (L, defined as $L = K_1/K_2$), magnetic foliation (F, defined as $F = K_2/K_3$), the shape factor (T, defined as $T = (2K_2 - K_1 - K_3) / (K_1 - K_3)$), and the degree of anisotropy (P, defined as $P = K_1/K_3$). The degree of AMS (Pj) and the alignment factor (F_s) are independent of sedimentation rate, sediment source, and sediment composition, and are calculated to constrain the flow pattern of the deep current.

Anisotropy degree (Pj) (Jelinek, 1981):

$$Pj = \exp \{2 \times [(\eta_1 - \eta_m)^2 + (\eta_2 - \eta_m)^2 + (\eta_3 - \eta_m)^2]\}^{1/2}$$

Alignment factor (F_s) (Ellwood, 1980):

$$F_s = K_1^2 / (K_2^2 \times K_3^2)^{1/2}$$

where η_1, η_2, and η_3 represent the logarithmic values of K_1, K_2, and K_3, respectively, and $\eta_m = (\eta_1 + \eta_2 + \eta_3)/3$.

In some cases, natural remanent magnetization declinations of cores can show apparent down-core trends, which are indicative of twisting during the coring process. Therefore, the mean ChRM was acquired for each core section in order to reorient the core to the geographical north according to Parés et al. (2007) (see Table S1). Where we observe an apparent trend in ChRM declinations, we estimate a linear trend line and calculate declination correction values for cube samples based on their relative position within the core. The deep circulation paleoflow is then determined based on statistical analysis of the azimuth of the K_1 axes calibrated with the mean ChRM (Table S1). This calibration method is more quantitative and efficient than traditional work-intensive optical measurements of the orientation of the grains (Wolff et al., 1989).

The preferential orientation of magnetic grains could be affected by several factors, including the Earth's gravity field, bottom current flows, and the geomagnetic field. The Earth's gravity field tends to cause mineral particles to be deposited with their larger surfaces paralleling the depositional surface (Zheng et al., 2016). In contrast, deposition from a bottom flow preferentially aligns the long axes of magnetic mineral grains parallel to the flow line. Although the geomagnetic field could orient the longer axes of the ferromagnetic grains to the local magnetic meridian, this effect mainly operates on fine grains that are not easily deposited when the bottom current is relatively strong. Therefore, the deposited magnetic grains are expected to record the intensity and orientation of the current rather than the orientation of the geomagnetic field (Li et al., 2019).

Rock magnetism

To characterize magnetic assemblages in representative samples, hysteresis loops, IRM acquisition curves, and back-field demagnetization curves were measured using a Princeton MicroMag vibrating sample magnetometer (VSM; Model 3900). Saturation magnetization (M_s), remanent saturation magnetization (M_{rs}), and coercivity (B_c) were determined after correction for the high-field slope representing the paramagnetic and diamagnetic components. The remanent coercivity (B_{cr}) was measured separately after applying stepwise increasing back-fields to $M_{rs.}$ IRM acquisition curves with 100 measurement points and non-linear field steps on a log scale up to 1.0 T were then obtained. In addition, in order to characterize the domain state and coercivity spectrum of magnetic minerals, first-order reversal curves (FORCs) for selected samples were measured using a VSM 3900 with field increment of 1.15 mT and processed with FORCinel software v1.18 (Harrison et al., 2018). All the magnetic measurements were conducted at the Geophysical Laboratory, Sun Yat-Sen University.

Light and heavy minerals analysis

After weighing the samples, the sample surfaces were cleaned and the organic matter was removed using 15% H_2O_2. After sufficient reaction, detrital minerals in the grain size range of 0.063-0.125 mm were screened out, and the samples were dried. The light and heavy minerals were separated from the dried samples with a heavy liquid separation method (using tribromomethane), and stereoscopic and polarized light microscopes were used to identify the light and heavy minerals, including quartz, hornblende, hypersthene, plagioclase, and volcanic glass. We identified over 300 grains in each subsample and counted them using a binocular microscope.

Spectral analysis

All data were linearly interpolated at 1 kyr intervals, and automatically detrended by the software prior to spectral analysis. In order to extract oscillations in the clay mineralogy and magnetic records associated with precession and obliquity periods (Figure 3), we applied Gaussian band-pass filters using the Acycle software (Li et al., 2019). The Gaussian band-pass filters were centred at 0.04762 kyr^{-1} (23-kyr cycle) with a band-width of 0.005 kyr^{-1} (20.62-25.98-kyr cycle) and at 0.02439 kyr^{-1} (41-kyr cycle) with a band-width of 0.005 kyr^{-1} (36.51-46.75-kyr).

Text S3 Sedimentological results

Clay mineralogy and geochemical composition

The clay mineral assemblage of core LV63-4-2 consists of dominant illite (37-69%, average 52%), moderate chlorite (16-46%, average 32%), and minor smectite (0-26%, average 8%) and kaolinite (1-18%, average 8%) (Figure S2b-e). Illite, chlorite, and smectite distributions display some variability through glacial-interglacial cycles, whereas there are no significant variations in kaolinite content. Illite content is generally anti-correlated with smectite, with slightly higher illite content during glacial intervals (particularly MIS 6) and higher smectite peaks occurring during interglacials (particularly MIS 1 and MIS 5.5). However, there is no simple link between these records and the LR04 benthic $\delta^{18}O$ stack (Lisiecki & Raymo, 2005) (Figure S2k). Since smectite and (illite + chlorite) distributions show inverse trends, the smectite / (illite + chlorite) ratio is used as an indicator of mineralogical changes in the clay fraction (Figure S2f). This mineralogical ratio ranges from 0 to 0.36, with lower values during glacial periods and higher values during interglacial periods. In addition, the warm sub-stages of MIS 5 (5.1, 5.3, 5.5) are also associated with higher smectite / (illite + chlorite) ratios (Figure S2f).

The ratios of Fe/Ca and Ti/Ca are typically used as proxies for siliciclastic flux relative to biogenic carbonate productivity. In general, Ca input from siliciclastic sources is relatively low, making the Ca content mostly a function of biogenic carbonate content (Govin et al. 2012). In core LV63-4-2, the Fe/Ca and Ti/Ca ratios covary over glacial-interglacial cycles, with low values during interglacials and high values during glacials (Figure S2g, h). Ratios of Rb/Sr and K/Al provide proxies for the degree of chemical weathering (Clift et al., 2020), although they are also sensitive to sediment grain-size. Here, K/Al and Rb/Sr ratios vary synchronously, with relatively higher values during glacials (particularly MIS 6), and lower values during interglacials (particularly MIS 1, 5.5, 7.1 and 7.3) (Figure S2i, j). Overall, these data can be explained by finer-grained clastic inputs during glacial periods, and by coarser and/or more extensively chemically weathered inputs during interglacials.

Temporal variations in magnetic parameters, light minerals and volcanic

glass

The downcore records of χ, χ_{ARM}, SIRM, and M_s, exhibit similar long-wavelength fluctuations (Figure S3a-d), with higher values indicating a higher content of magnetic minerals. However, there is no clear relationship between these parameters and the LR04 benthic $\delta^{18}O$ stack (Figure 3m).

Since the low coercivity minerals dominate the magnetic signal, the ratios of χ_{ARM}/χ and χ_{ARM}/SIRM are commonly used as proxies for the magnetic grain size of ferrimagnetic particles (Peters & Dekkers, 2003). In general, higher values of χ_{ARM}/χ and χ_{ARM}/SIRM correspond to a finer magnetic grain size (Figure S3e, f). Although all samples fall within a limited range of magnetic grain size, it is notable that high values of χ_{ARM}/χ and χ_{ARM}/SIRM (finer grain size) tend to occur during glacial intervals, with lower values (coarser grain size) during interglacials (Figure S3e, f). In particular, the mean values for both parameters are at their highest values of the record during the Last Glacial Maximum (MIS 2).

The $HIRM_{300mT}$ and S-ratio quantify the absolute and relative concentration of high coercivity minerals, respectively (Liu et al., 2012). The temporal variations of $HIRM_{300mT}$ (Figure S3g) are generally similar to variability in χ_{ARM} and SIRM. Higher S-ratios indicate a higher relative abundance of low coercivity minerals (Liu et al., 2007). The S-ratios of core LV63-4-2 are generally between 0.94 and 1, and almost always greater than 0.9, indicating the dominance of low coercivity magnetic minerals (e.g. magnetite) in the core (Figure S3h). The L-ratios are in the range of 0.04 to 0.2 and show a similar but inverse trend to the S-ratios (Figure S3h, i). These fluctuations in $HIRM_{300mT}$, S-ratio, and L-ratio (Figure S3g-i) indicate increases in high coercivity minerals during interglacial intervals and decreases during glacials. Furthermore, these variations were generally closely linked to variations in the grain size of the ferrimagnetic minerals (Figure S3e, f), with increased proportions of low coercivity minerals during glacials coinciding with finer magnetic grain sizes. FORC diagrams indicate that samples selected from MIS 2 to MIS 5 have comparable distributions and are dominated by vortex state. In contrast, the sample selected from MIS 1 shows weak distributions at low B_c field, which is likely due to a lack of low coercivity magnetic minerals (Figure S3n-p).

Considering the light minerals, the contents of quartz and plagioclase vary between 19 and 74% and 10 and 69 %, respectively, with higher mean values of both minerals during glacial periods (Figure S3j, k). Volcanic glasses range from 0 to 67 %, with significantly increased proportions during interglacial periods in contrast to low or zero abundance during glacial periods (Figure S3l).

Magnetic fabric

The magnetic foliation (*F*) is generally larger than the magnetic lineation (*L*), which suggests that K_1 is approximately equivalent to K_2, while K_1 and K_2 are larger than K_3 (Figure S4a). In terms of orientation, K_3 is perpendicular to the plane, while K_1 is parallel to the plane (Figure S4c). The shape of the magnetic susceptibility ellipsoid is largely oblate (Figure S4b), consistent with normal current-influenced sedimentation in the deep sea.

In such a case, the inclination and declination of the principal axes of the ellipsoid can potentially reveal information about the nature of deposition, while changes in *Pj* and *Fs* have also been linked to both flow speed and to sediment composition (Yokokawa & Franz, 2002). For core LV63-4-2, the inclinations of K_1 and K_3, *Pj* values, and *Fs* values are shown in Figure S5, which demonstrates that the directional AMS data do not appear to be related to the degree of anisotropy. Throughout the core, *Pj* and *Fs* values increase slowly with depth, which suggests that they represent the effect of sedimentary compaction rather than a current-induced lineation (Figure S5b, c). In contrast, we suggest that the high amplitude variations in the inclination of K_1 and K_3 within the glacial sections of the core indicate the operation of a strong hydrodynamic force during glacial periods (Figure S5a). Because magnetite is the dominant magnetic mineral in the core and it has weak crystalline anisotropy, the orientation of the magnetic susceptibility ellipsoid is dominated by the alignment of the long axes of magnetite grains (Kissel et al., 2010). Therefore, the general trend of the long axes of magnetic fabric can be taken to indicate the paleo-flow direction in core LV63-4-2.

Other influences such as the slope at the depositional site, coring/sampling disturbance, and downslope movement could also lead to deviations in K_1 declination. For example, downslope movements could potentially generate random directions in certain intervals. However, the *F-L* and *P-T* plots suggest that these possibilities are unlikely, and demonstrate that current activity is not restricted to certain K_1 declination directions (Figure S4). Although a stronger current may potentially lead to grains being deposited with their K_1 declination perpendicular to flow, this situation probably mainly occurs in non-Newtonian fluids (Novak et al., 2014; Tauxe et al., 1998).

A rose diagram of the calibrated declinations of K_1 indicates that the major azimuths in the full dataset are 45° (i.e. NE-SW) and 190° (i.e. approximately S-N) (Figure S4d). In addition, there are also glacial-interglacial variations in azimuth, as well as differences between individual glacials and interglacials (Figure 2). During MIS 1, the calibrated declination of K_1 has the main azimuths of ~135° (SE-NW), in agreement with the dominant directions of the deep currents in the modern western North Pacific Ocean (Owens & Warren, 2001) (Figure 1b). In contrast, for the previous warm periods of MIS 3 and MIS 5, the azimuth was NE-SW. During past glacials, the flow direction was also different from the modern day, with an approximately S-N azimuth during MIS 4 and MIS 6. During MIS 2, the high amplitude variations in inclination (Figure S5a) and widely-varying azimuth directions for K_1 suggest a high current velocity and potentially variable flow directions (Figure 2a).

Supplementary References

Supplementary References

Barker, S., Knorr, G., Edward, R. L., Parrenin, F., Putnam, A. E., Skinner, L. C., et al. (2011). 800,000 years of abrupt climate variability. *Science*, *334*, 347-351.

Biscaye, P. E. (1965). Mineralogy and sedimentation of recent deep-sea clay in the Atlantic Ocean and adjacent seas and oceans, *Geological Society America Bulletin*, *76*, 803-832.

Cavalieri, D. J. & Martin, S. (1994). The contribution of Alaskan, Siberian, and Canadian coastal polynas to the cold halocline layer of the Arctic Ocean. *Journal of Geophysical Research Oceans*, *99*, 18343-18362.

Cheng, H., Edwards, R. L., Sinha, A., Spötl, C., Yi, L., Chen, S., et al. (2016). The Asian monsoon over the past 640,000 years and ice age terminations. *Nature*, *534*, 640-646.

Clift, P. D., Kulhanek, D. K., Zhou, P., Bowen, M. G., Vincent, S. M., Lyle, M., & Hahn, A. (2020). Chemical weathering and erosion responses to changing monsoon climate in the Late Miocene of Southwest Asia. *Geological Magazine*, *157*, 939-955.

Danielson, S. L., Weingartner, T. J., Hedstrom, K. S., Aagaard, K., Woodgate, R., Curchitser, E., & Stabeno, P. J. (2014). Coupled wind-forced controls of the Bering-Chukchi shelf circulation and the Bering Strait throughflow: Ekman transport, continental shelf waves, and variations of the Pacific-Arctic sea surface height gradient. *Progress in Oceanography*, *125*, 40-61.

Ellwood, B. B. (1980). Application of the anisotropy of magnetic susceptibility method as an indicator of bottom-water flow direction, *Marine Geology*, *34*(3), 83-90.

Govin, A., Holzwarth, U., Heslop, D., Ford Keeling, L., Zabel, M., Mulitza, S., Collins, J. A., Chiessi, C, M. (2012). Distribution of major elements in Atlantic surface sediments (36°N-49°S): Imprint of terrigenous input and continental weathering. *Geochemistry, Geophysics, Geosystems*, *13*, Q01013.

Harrison, R. J., Muraszko, J., Heslop, D., Lascu, I., Muxworthy, A. R., & Roberts, A. P. (2018). An Improved Algorithm for Unmixing First-Order Reversal Curve Diagrams Using Principal Component Analysis. *Geochemistry, Geophysics, Geosystems*, *19*, 1595-1610.

Hrouda, F. (1982). Magnetic anisotropy of rocks and its application in geology and geophysics. *Geophysical Surveys*, *5*, 37-82.

Jelinek, V. (1981). Characterization of the magnetic fabric of rocks. *Tectonophysics*, *79*(3), 63-67.

King, J. W. & Channell, J. E. T. (1991). Sedimentary magnetism, environmental magnetism, and magnetostratigraphy. *Reviews of Geophysics*, *29*, 358-370.

Kissel, C., Laj, C., Kienast, M., Bolliet, T., Holborn, A., Hill, P., et al. (2010). Monsoon variability and deep oceanic circulation in the western equatorial Pacific over the last climatic cycle: Insights from sedimentary magnetic properties and sortable silt. *Paleoceanography*, 25, PA3215.

Kwon, Y. O., Alexander, M. A., Bond, N. A., Frankignoul, C., Nakamura, H., Qiu, B., & Thompson, L. A. (2010). Role of the Gulf Stream and Kuroshio-Oyashio systems in large-scale atmosphere-ocean interaction: A review. *Journal of Climate*, *23*(12), 3249-3281.

Li, M. S. Hinnov, L. & Kump, L. (2019). A-cycle: Time-series analysis software for paleoclimate research and education. *Computers & Geosciences*, *127*, 12-22.

Lisiecki, L. E. & Raymo, M. E. (2005). A Pliocene−Pleistocene stack of 57 globally distributed benthic $\delta^{18}O$ records. *Paleoceanography*, *20*(1), PA1003.

Liu, Q. S., Roberts, A. P., Torrent, J., Horng, C S., & Larrasoaña, J. C. (2007). What do the HIRM and S-ratio really measure in environmental magnetism? *Geochemistry, Geophysics, Geosystems*, *8*, Q0911.

Liu, Q. S., Roberts, A. P., Larrasoana, J. C., Banerjee, S. K., Guyodo, Y., Tauxe, L., & Oldfield, F. (2012). Environmental magnetism: principles and applications. *Reviews of Geophysics*, *50*, RG4002.

Lougheed, B. C. & Obrochta, S. P. (2019). A rapid, deterministic age-depth modeling routine for geological sequences with inherent depth uncertainty. *Paleoceanography and Paleoclimatology*, *34*(1), 122-133.

Luchin, V. A., Semiletov, I. P. & Weller, G. E. (2002). Changes in the Bering Sea region: atmosphere-ice-water system in the second half of the twentieth century. *Progress in Oceanography*, *55*, 23-44.

Moore, D. M., & Reynolds, R. C. (1989). X-ray Diffraction and the identification and analysis of clay minerals, Oxford Univ. Press, Oxford.

Nagashima, K., Asahara, Y., Takeuchi, F., Harada, N., Toyoda, S., & Tada, R. (2012). Contribution of detrital materials from the Yukon River to the continental shelf sediments of the Bering Sea based on the electron spin resonance signal intensity and crystallinity of quartz. *Deep Sea Research Part II: Topical Studies in Oceanography*, *61-64*, 145-154.

Naidu, A. S., Han, M. W., Mowatt, T. C. & Wajda, W. (1995). Clay minerals as indicators of sources of terrigenous sediments, their transportation and deposition: Bering Basin, Russian-Alaskan Arctic. *Marine Geology*, *127*, 87-104.

Nakanowatari, T. Nakamura, T., Uchimoto, K., Nishioka, J., Mitsudera, H., & Wakatsuchi, M. (2017). Importance of Ekman transport and gyre circulation change on seasonal variation of surface dissolved iron in the western subarctic North Pacific. *Journal of Geophysical Research: Oceans*, 122(5), 4364-4391.

Niebauer, H. J., Bond, N. A., Yakunin, L. P., & Plotnikov, V. V. (1999).An update on the climatology and sea ice of the Bering Sea. In: Loughlin, T. R. and K. Ohtani (Eds.), The Bering Sea: a Summary of Physical, Chemical and Biological Characteristics and a Synopsis of Research. North Pacific Marine Science Organization, PICES, Alaska Sea Grant Press, 29-59.

Novak, B., Housen, B., Kitamura, Y., Kanamatsu, T. & Kawamura, K. (2014). Magnetic fabric analyses as a method for determining sediment transport and deposition in the deep-sea sediments. *Marine Geology*, *356*, 19-30.

Owens, W. B. & Warren, B. A. Deep circulation in the northwest corner of the Pacific Ocean. (2001). *Deep-Sea Research-Oceanographic Research Papers*, *48*, 959-993.

Parés, J.M., Hassold, N. J. C., Rea, D. K. & van der Pluijm, B. A. (2007). Paleocurrent directions from paleomagnetic reorientation of magnetic fabrics in deep-sea sediments at the Antarctic Peninsula Pacific margin (ODP Sites 1095, 1101). *Marine Geology*, *242*, 261-269.

Peters, C. & Dekkers, M. J. (2003). Selected room temperature magnetic parameters as a function of mineralogy, concentration and grain size. *Physics and Chemistry of the Earth*, *28*, 659-667.

Qiu, B. (2002). Large-scale variability in the midlatitude subtropical and subpolar North Pacific Ocean: Observations and causes. *J. Phys. Oceanogr*, *32*, 353-375.

Reimer, P. J. (2013). Intcal 13 and Marine-13 radiocarbon age calibration curves 0-50,000 years cal BP. *Radiocarbon*, *55*(4), 1869-1887.

Riethdorf, J. R. Thibodeau, B., Ikehara, M., Nürnberg, D., Max, L., Tiedemann, R., & Yokoyama, Y. (2016). Surface nitrate utilization in the Bering sea since 180 ka BP: Insight from sedimentary nitrogen isotopes. *Deep Sea Research Part II Topical Studies in Oceanography*, *125*, 163-176.

Roden, G. I. (1995). Aleutian Basin of the Bering Sea: Thermohaline, oxygen, nutrient, and current structure in July 1993. Journal of Geophysical Research Oceans, 100, 13539-13554.

Schlung, S. A., Ravelo, A. C., Aiello, I. W., Andreasen, D. H., Cook, M. S., Drake, M., et al. (2013). Millennial-scale climate change and intermediate water circulation in the Bering Sea from 90 ka: A high-resolution record from IODP Site U1340. *Paleoceanography*, *28*(1), 54-67.

Schumacher, J. D., Aagaard, K., Pease, C. H., & Tripp, R. B. (1983). Effects of a Shelf Polynya on Flow and Water Properties in the Northern Bering Sea. *Journal of Geophysical Research Oceans 88*, 2723-2732.

Stabeno, P. J., Schumacher, J. D., & Ohtani, K. (1999). The physical oceanography of the Bering Sea. In: Loughlin, T. R. and K. Ohtani (Eds.), The Bering Sea: a Summary of Physcial, Chemical and Biological Characteristics and a Synopsis of Research. North Pacific Marine Science Organization, PICES, Alaska Sea Grant Press, 1-28.

Stabeno, P. J., Bell, S., Cheng, W., Danielson, S., Kachel, N. B., & Mordy, C. W.Stabeno, P. J. (2016). Long-term observations of Alaska Coastal Current in the northern Gulf of Alaska. *Deep Sea Research Part II: Topical Studies in Oceanography*, *132*, 24-40.

Stabeno, P. J. & Bell, S. W. (2019). Extreme conditions in the Bering Sea (2017-2018): record-breaking low sea-ice extent. *Geophysical Research Letters, 46*(15), 8952-8959.

Tauxe, L., Gee, J. S. & Stadigel, H. (1998). Flow directions in dikes from anisotropy of magnetic susceptibility data: The bootstrap way. *Journal of Geophysical Research*: *Solid Earth*, *103*(B8), 17775-17790.

Wang, R., Biskaborn, B. K., Ramisch, A., Ren, J., Zhang, Y. Z., Gersonde, R., & Diekmann, B. (2016). Modern modes of provenance and dispersal of terrigenous sediments in the North Pacific and Bering Sea: implications and perspectives for palaeoenvironmental reconstructions. *Geo-Marine Letters*, *36*, 259-270.

Wolff, J. A., Ellwood, B. B. & Sachs, S. D. (1989). Anisotropy of magnetic susceptibility in welded tuffs: application to a welded-tuff dyke in the tertiary Trans-Pecos Texas volcanic province, USA. *Bulletin of Volcanology*, *51*, 299-310.

Yokokawa, M. & Franz, S. O. (2002). Changes in grain size and magnetic fabric at Blake-Bahama Outer Ridge during the late Pleistocene (marine isotope stages 8-10). *Marine Geology*, *189*, 123-144.

Yuan, X. & Talley, L. D. (1996). The subarctic frontal zone in the North Pacific: Characteristics of frontal structure from climatological data and synoptic surveys. *Journal of Geophysical Research Oceans*, *101*, 16491-16508.

Zheng, X. F., Kao, S. J., Chen, Z., Menviel, L., Chen, H., Du, Y., et al. (2016). Deepwater circulation variation in the South China Sea since the Last Glacial Maximum. *Geophysical Research Letters*, *43*, 8590-8599.

Zhong, Y., Liu, Y. G., Yang, X. Q., Zhang, J., Liu, J. B., Bosin, A. et al. (2020). Do non-dipole geomagentic field behaviors persistently exist in the subarctic Pacific Ocean over the past 140 ka? *Science Bulletin*, *65*, 1505-1507.

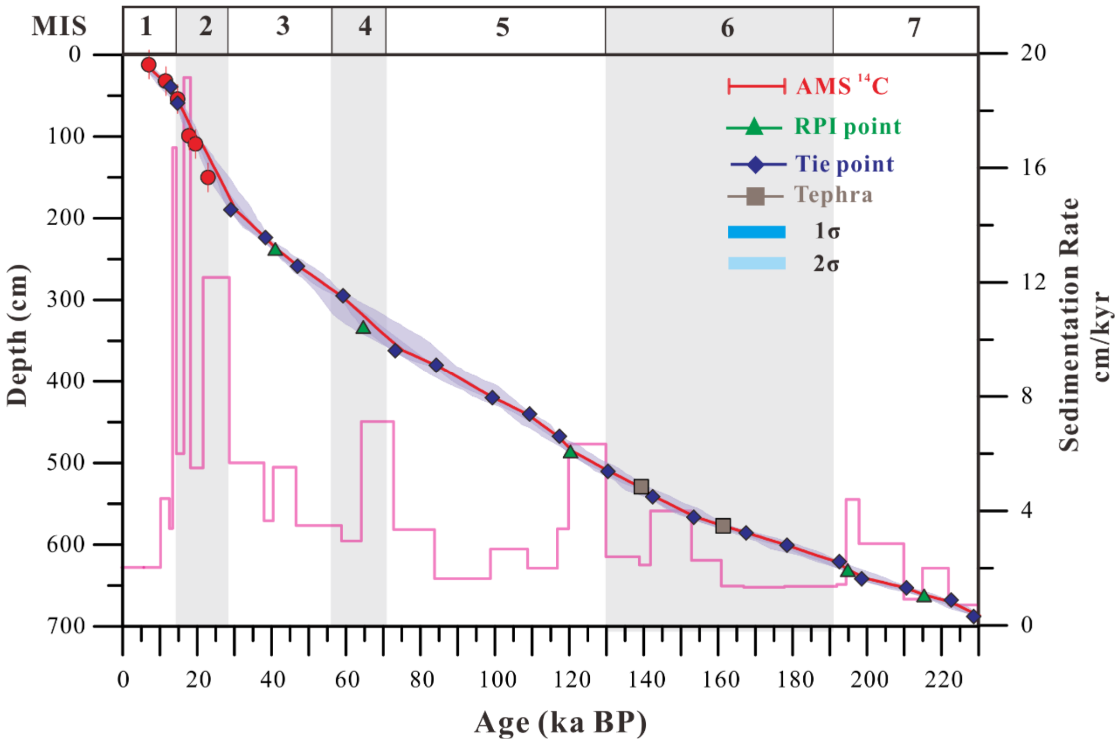

Fig. S1. Age-depth model for core LV63-4-2. Tie points were based on correlation between XRF fluorescence or colour L* in LV63-4-2 and $\delta^{18}O$ records from the NGRIP ice core (Barker et al., 2011) and Sanbao stalagmites (Cheng et al., 2016). These assignments were validated by magnetostratigraphy (relative paleointensity, RPI), tephra ages, and accelerator mass spectrometry (AMS) radiocarbon ages on planktonic foraminifera. The radiocarbon ages from core LV63-4-2 were recalibrated using MARINE13 (Reimer, 2013) and uncertainties are indicated by red error bars. Sedimentation rates varied from ~1 cm/kyr to ~19 cm/kyr. The 1σ and 2σ age uncertainties were estimated using the Undatable software package (Lougheed & Obrochta, 2019). See Zhong et al. (2020) for full details of the age model. Grey bars indicate glacial periods.

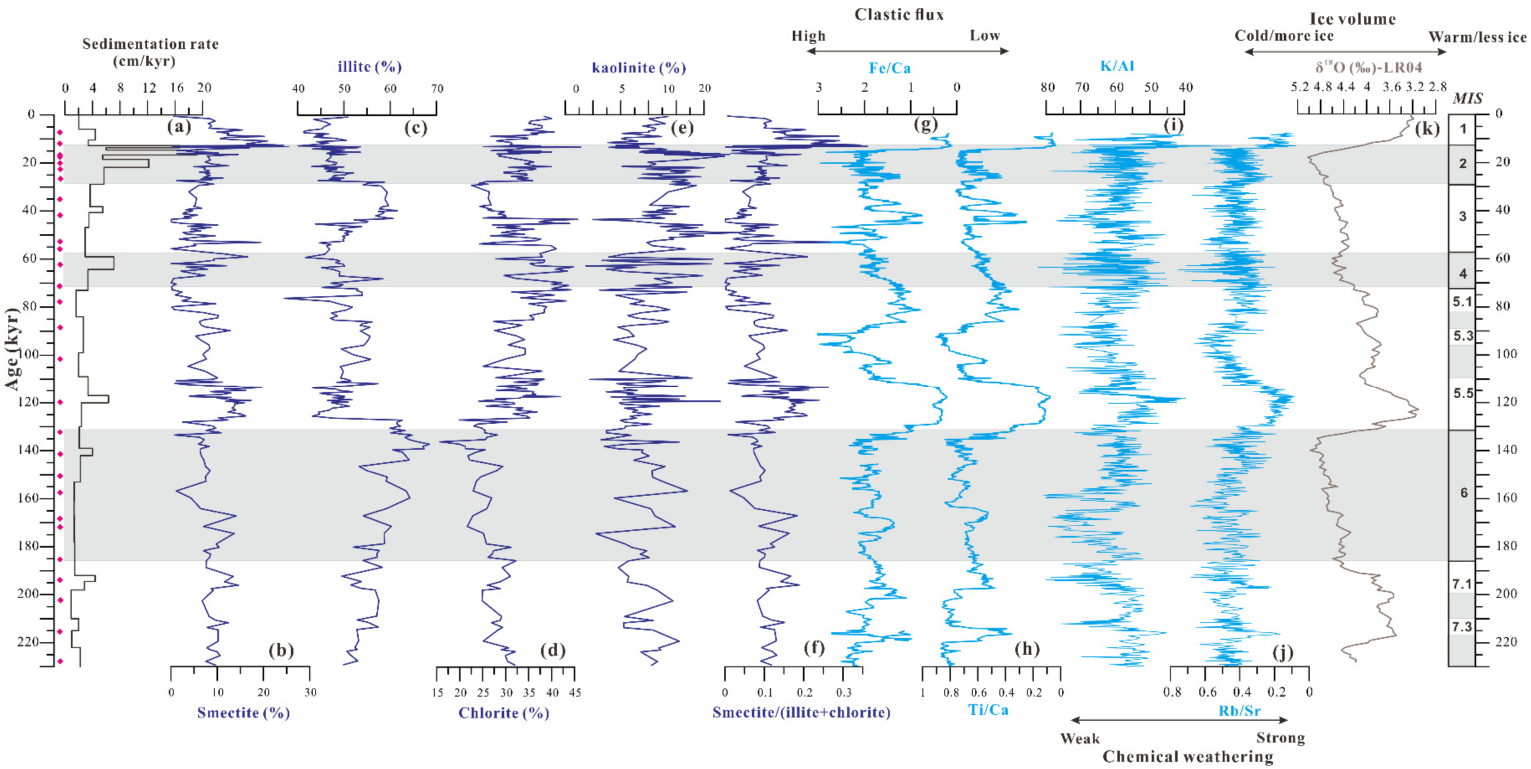

Fig. S2. Temporal variations in clay mineralogy and elemental chemistry in core LV63-4-2 since 230 ka BP: (a) sedimentation rate (cm/kyr); (b-e) clay mineral proportions (%) in the <2 µm size fraction; (f) smectite/(illite + chlorite) ratio; (g-h) Fe/Ca and Ti/Ca ratios from XRF-scanning as an indicator of clastic versus carbonate sedimentation; (i-j) K/Al and Rb/Sr ratios from XRF-scanning as an indicator of chemical weathering intensity and/or grain size of the supplied sediments; (k) LR04 benthic $\delta^{18}O$ stack (Lisiecki & Raymo, 2005) . Grey bars indicate glacial periods.

Fig. S3.

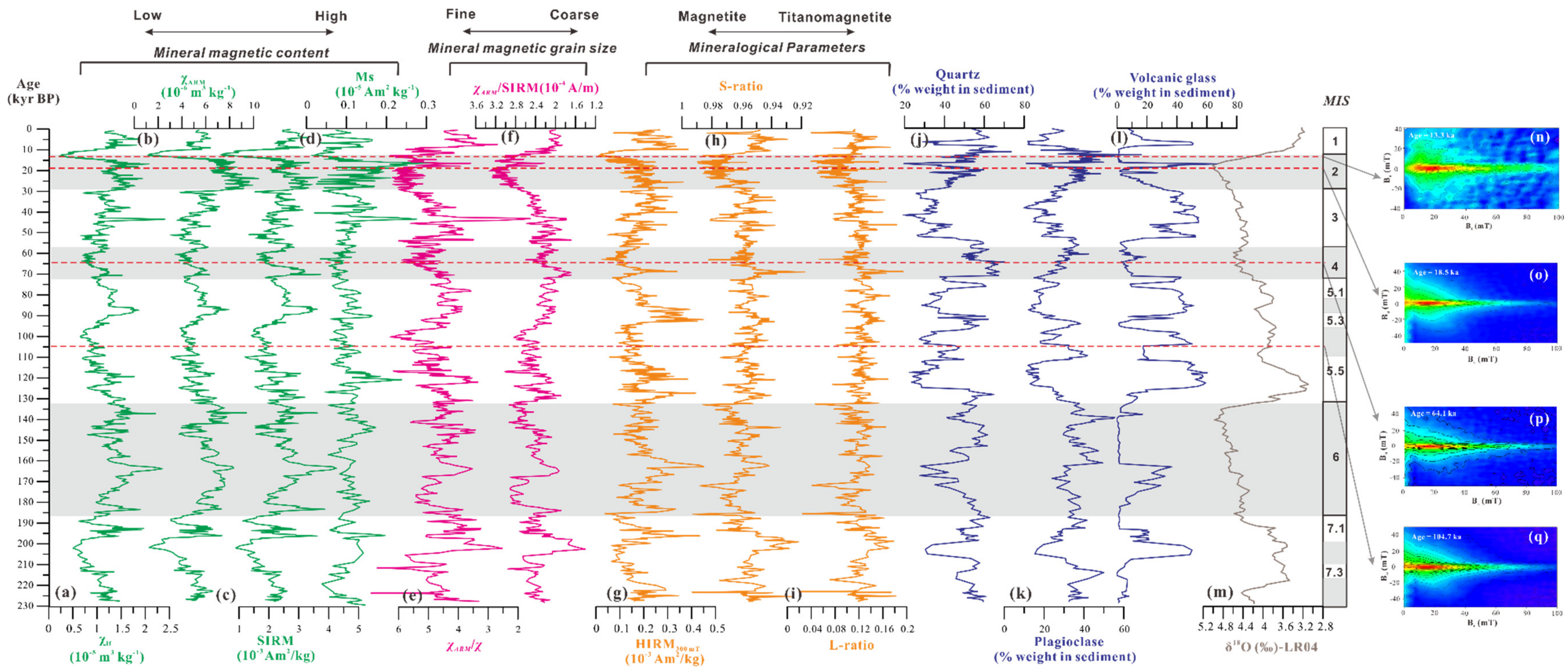

Fig. S3. Temporal variations in magnetic parameters and representative mineral abundances in core LV63-4-2 since 230 ka BP: (a) χ_{lf}, low-frequency susceptibility; (b) χ_{ARM}, anhysteretic remanent magnetization susceptibility; (c) SIRM$_{1.0\ T}$, saturation isothermal remanent magnetization; (d) M_S, saturation magnetization; (e) χ_{ARM}/χ; (f) χ_{ARM}/SIRM; (g) HIRM$_{300mT}$; (h) S-ratio; (i) L-ratio; (j) quartz (weight % in sediment); (k) plagioclase (weight % in sediment); (l) volcanic glass (weight % in sediment); (m) LR04 benthic $\delta^{18}O$ stack (Lisiecki & Raymo, 2005). Grey bars indicate glacial periods. (n-q) FORC diagrams indicate that samples selected from MIS 2 to MIS 5 have comparable distributions and are dominated by vortex state. In contrast, the sample selected from MIS 1 shows weak distributions at low B_c field, which is likely due to the lack of low coercivity magnetic minerals.

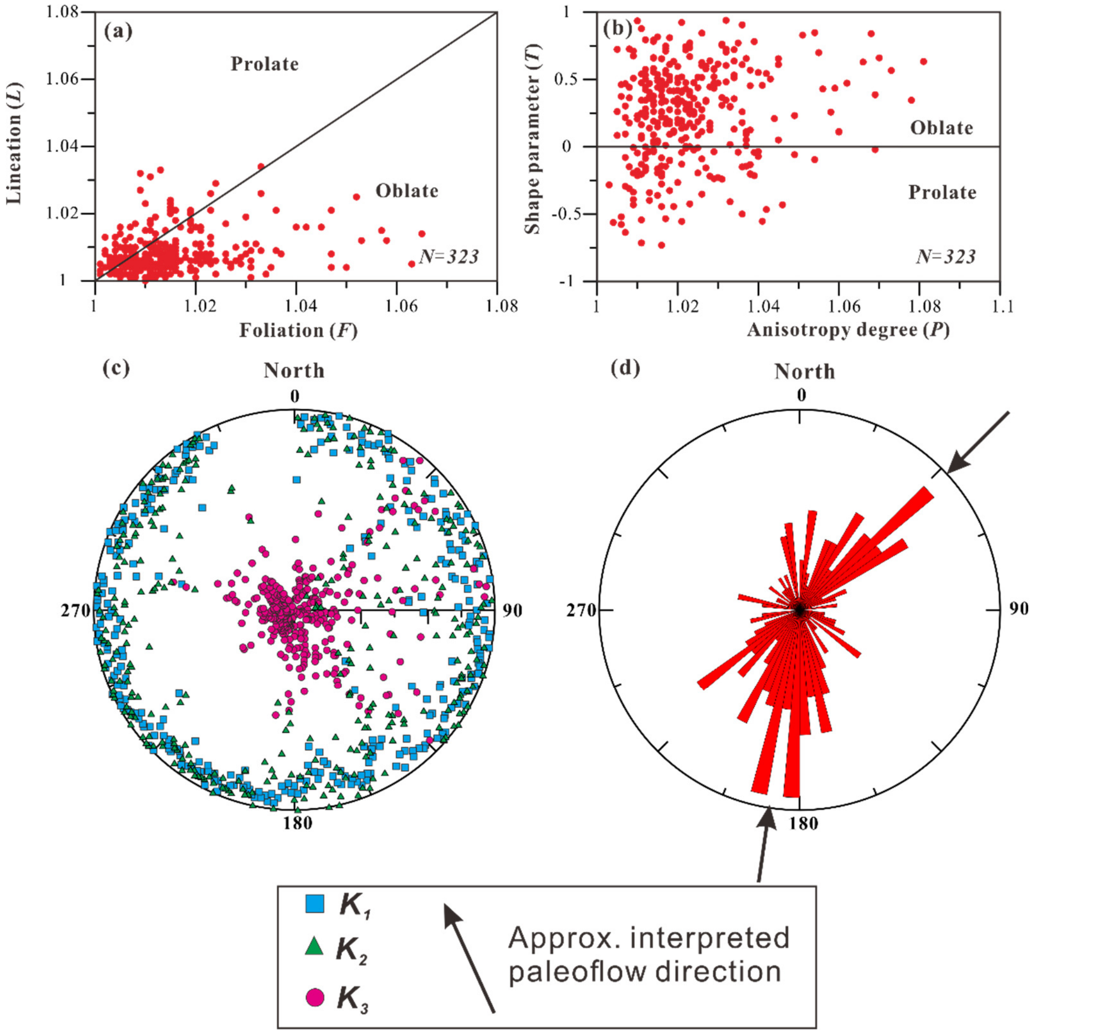

Fig. S4. Anisotropy of magnetic susceptibility (AMS) data from core LV63-4-2: (a) magnetic lineation (L) versus magnetic foliation (F); (b) shape factor (T) versus degree of anisotropy (P); (c) stereonet projection of the maximum (K_1), intermediate (K_2), and minimum (K_3) susceptibility axes; (d) rose diagram of the azimuth of K_1. Data comprise 323 samples.

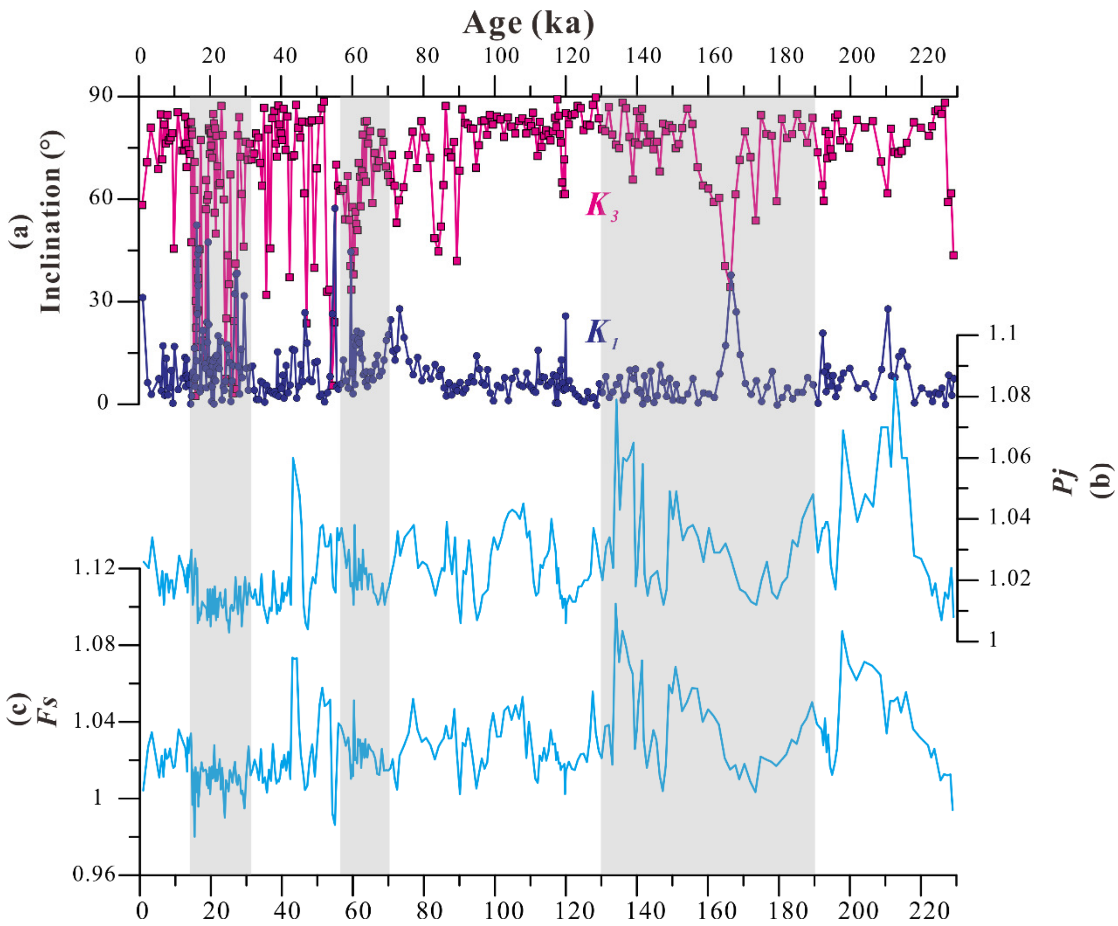

Fig. S5. Temporal variations in selected magnetic fabric parameters in core LV63-4-2: (a) inclination of K_1 (blue circles) and K_3 (pink squares); (b) anisotropy degree (*Pj*); (c) alignment factor (*Fs*). Grey bars indicate glacial periods.

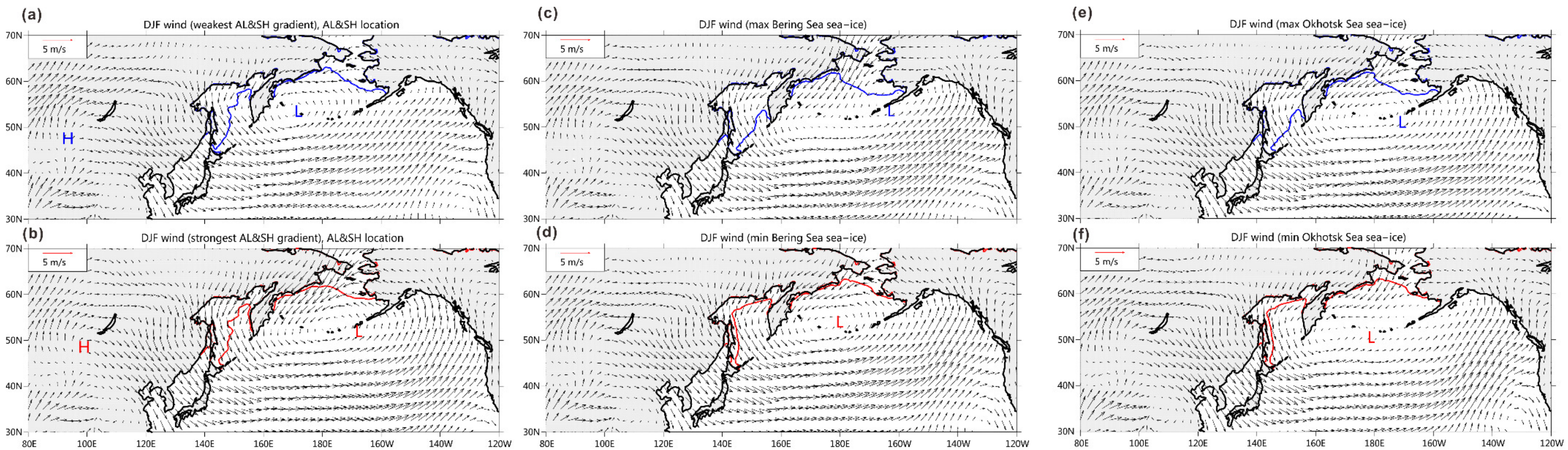

Fig. S6. Reanalysis data from 1979-2017 showing 5-year composites of February sea-ice extent and winter (DJF) AL location (marker L), and low-level (850-1000 hPa) wind (arrows). (a, b) weakest and strongest SH versus AL pressure gradient; (c, d) maximum and minimum Bering Sea sea-ice extent; (e, f) maximum and minimum sea-ice extent in the Sea of Okhotsk.

Table S1. Summary of mean characteristic remanent magnetization (ChRM) parameters for each section and calculated calibrated angle.

Section	Depth (cm)	Sample Number	Mean ChRM inclination	Mean ChRM declination	Angle for remanence measuring placement	Calibrated angle*
1	0~88	32	58.4°	216.2°	+180°	-36.2°
2	88~184	45	52.4°	171.4°		8.6°
3	184~285	49	49.3°	117.5°		62.5°
4	285~385	49	37.6°	180.5°		-0.5°
5	385~485	49	63.2°	119.1°		60.9°
6	485~586	50	44.6°	148.8°		31.2°
7	586~685	49	65.8°	210.0°		-30.0°

*, + = clockwise; - = anticlockwise.